Journal of Medicinal Chemistry

Article

A Kinome-Wide Selective Radiolabeled TrkB/C Inhibitor for in Vitro and in Vivo Neuroimaging: Synthesis, Preclinical Evaluation and First-in-Human

Vadim Bernard-Gauthier, Justin J. Bailey, Andrew V. Mossine, Simon Klaus Lindner, Lena Vomacka, Arturo Aliaga, Xia Shao, Carole A. Quesada, Phillip S. Sherman, Anne Mahringer, Alexey Kostikov, Marilyn Grand'Maison, Pedro Rosa-Neto, Jean-Paul Soucy, Alexander Thiel, David R. Kaplan, Gert Fricker, Björn Wängler, Peter Bartenstein, Ralf Schirrmacher, and Peter J. H. Scott

J. Med. Chem., **Just Accepted Manuscript** • DOI: 10.1021/acs.jmedchem.7b00396 • Publication Date (Web): 11 Jul 2017

A Kinome-Wide Selective Radiolabeled TrkB/C Inhibitor for *in Vitro* and *in Vivo* Neuroimaging: Synthesis, Preclinical Evaluation and First-in-Human

Vadim Bernard-Gauthier[a,1], Justin J. Bailey[a], Andrew V. Mossine[b], Simon Lindner[c], Lena Vomacka[c], Arturo Aliaga[d], Xia Shao[b], Carole A. Quesada[b], Phillip Sherman[b], Anne Mahringer[e], Alexey Kostikov[f], Marilyn Grand'Maison[g], Pedro Rosa-Neto[d], Jean-Paul Soucy[h], Alexander Thiel[f,i], David R. Kaplan[j,k], Gert Fricker[e], Björn Wängler[l], Peter Bartenstein[c], Ralf Schirrmacher[a,1,2*], Peter J. H. Scott[b,m,2]*

[a]Department of Oncology, Division of Oncological Imaging, University of Alberta, Edmonton, AB, T6G 2R3, Canada.

[b]Division of Nuclear Medicine, Department of Radiology, The University of Michigan Medical School, Ann Arbor, MI, 48109, United States.

[c]Department of Nuclear Medicine, Ludwig-Maximilians-University of Munich, Marchioninistr. 15, Munich, 81377, Germany.

[d]Translational Neuroimaging Laboratory, McGill Centre for Studies in Aging, Douglas Mental Health University Institute, 6875 Boulevard LaSalle, Montreal, QC, H4H 1R3, Canada.

[e]Institute of Pharmacy and Molecular Biotechnology, University of Heidelberg, Heidelberg 69120, Germany.

[f]McConnell Brain Imaging Centre, Montreal Neurological Institute, McGill University, 3801 University Street, Montreal, QC, H3A 2B4, Canada.

[g]Biospective Inc., 6100 Avenue Royalmount, Montreal, QC H4P 2R2, Canada.

[h]Department of Neurology and Neurosurgery, Montreal Neurological Institute, McGill University, 3801 University Street, Montreal, QC, H3A 2B4, Canada.

[i]Jewish General Hospital, Lady Davis Institute, Montreal, QC, HT3 1E2, Canada.

[j]Program in Neurosciences and Mental Health, Hospital for Sick Children, Toronto, ON, M5G 0A4, Canada.

[k]Department of Molecular Genetics, University of Toronto, ON, M5S1A8, Canada

[l]Molecular Imaging and Radiochemistry, Department of Clinical Radiology and Nuclear Medicine, Medical Faculty Mannheim of Heidelberg University, Theodor-Kutzer-Ufer 1-3, Mannheim 68167, Germany.

[m]The Interdepartmental Program in Medicinal Chemistry, University of Michigan, Ann Arbor, MI 48109, United States.

[1]Corresponding authors:

[2]P.J.H.S. and R.S. contributed equally to this work.

Keywords: Tropomyosin receptor kinases, Trk, positron emission tomography, PET, neuroimaging, tyrosine kinase inhibitor, Alzheimer's disease, *NTRK*.

ABSTRACT

The proto-oncogenes *NTRK1/2/3* encode the tropomyosin receptor kinases TrkA/B/C which play pivotal roles in neurobiology and cancer. We describe herein the discovery of [^{11}C]-(*R*)-**3** ([^{11}C]-(*R*)-IPMICF16), a first-in-class positron emission tomography (PET) TrkB/C-targeting radiolabeled kinase inhibitor lead. Relying on extensive human kinome vetting, we show that (*R*)-**3** is the most potent and most selective TrkB/C inhibitor characterized to date. It is demonstrated that [^{11}C]-(*R*)-**3** readily crosses the blood-brain barrier (BBB) in rodents and selectively binds to TrkB/C receptors *in vivo,* as evidenced by entrectinib blocking studies. Substantial TrkB/C-specific binding in human brain tissue is observed *in vitro*, with specific reduction in the hippocampus of Alzheimer's disease (AD) versus healthy brains. We additionally provide preliminary translational data regarding the brain disposition of [^{11}C]-(*R*)-**3** in primates including first-in-human assessment. These results illustrate for the first time the use of a kinome-wide selective radioactive chemical probe for endogenous kinase PET neuroimaging in human.

INTRODUCTION

Specific interaction between the full-length catalytic tropomyosin receptor kinases TrkA/B/C (encoded by *NTRK1-3* respectively) and their cognate neurotrophin ligands (nerve growth factor (NGF), brain-derived neurotrophic factor (BDNF) and neurotrophin-3 (NT-3), respectively) crucially supports differentiation, growth and survival within distinct neuronal populations of the mammalian central (CNS) and peripheral nervous systems (PNS) as well as non-neural tissues during development and adult life.[1-3] Reduced expression or impaired signaling of Trk tyrosine kinase (TK) receptors in the CNS is found in an extensive spectrum of disorders and pathologies including ischemic brain injury, schizophrenia, Rett syndrome, depression and various neurodegenerative diseases.[2-14] In addition to their central roles in neurobiology, all three members of the Trk family are proto-oncoproteins with well-defined oncogenic potential in human, both in neural and non-neural neoplasms.[15-19] So far, the validation of Trk changes during aging and neurodegenerative diseases has solely originated from studies relying on immunohistochemical (IHC) detection and *in situ* hybridization (ISH) of post-mortem tissue[11-13, 20-24] while preclinical assessment of brain exposure for anticancer Trk inhibitors (**Figure 1** and **Table S1**) has been circumscribed to the use of destructive methods[25-26] due to the absence of a non-invasive approach to assess and quantify Trk levels *in vivo.*

Quantitative neuroimaging of proteins in humans using positron emission tomography (PET) is a robust *in vivo* approach which relies on short-lived radiolabeled small molecules.[27] Most clinical CNS radiotracers validated to date target G protein-coupled receptors (GPCR), ion channels, transporters and abnormally conformed proteins.[28] Clinical neuroimaging of CNS endogenous kinases has not yet been achieved despite key realisations in a few other enzyme classes.[28-30] Given the importance of Trk (especially TrkB/C, which are most abundant in the CNS and expressed in overlapping neuron populations), we sought to develop a radiolabeled targeted kinase inhibitor for PET imaging to enable the visualisation and quantification of TrkB/C

receptor density in healthy and diseased brains. An important advantage of the selection of a radiolabeled tyrosine kinase inhibitor (TKI) rather than an extracellular binding compound resides in the intrinsic capacity of such probes to dissect pro-survival neuronal full-length TrkB/C receptors from catalytically-incompetent truncated isoforms (most notably TrkB.T1) largely present in glia.[31-32]

Herein, we describe our radiotracer development effort in the assessment of [^{11}C]-(*R*)-**3** ([^{11}C]-(*R*)-IPMICF16) as a first-in-class brain penetrating TrkB/C-targeted lead for PET neuroimaging (**Figure 1**). The work presented includes the radiotracer structure-activity relationship (SAR) characterization and comparative analysis leading to [^{11}C]-(*R*)-**3**, the enantioselective synthesis of (*R*)-**3** and labeling precursor thereof, as well as the entire *in vivo* imaging translational work in four species from early evaluation in rats and mice, preclinical non-human primates as well as first-in-human clinical PET imaging. We concomitantly provide proof-of-principle of *in vivo* TrkB/C target engagement in the living brain for [^{11}C]-(*R*)-**3** and TrkB/C receptor occupancy with pharmacological pre-dosing of the phase II clinical lead entrectinib using imaging experiments in mice. Particularly, we also demonstrate that the radiotracer displays high TrkB/C-specific binding in human brain tissue and observes a distinct regional binding pattern in Alzheimer's disease (AD) versus healthy control (HC) *in vitro*.

RESULTS

Chemistry, biochemical evaluations and radiochemistry. Optimal compound triage for the development of neuroimaging PET radioligands entails the alignment of favorable physicochemical properties (molecular weight (MW) < 500 Da, topological polar surface area (TPSA) ≤ 80 Å^2, hydrogen bond donor (HBD) ≤ 1, 2 ≤ clogD < 4, 3 ≤ clogP < 5, pK_a ≤ 8, rotatable bonds (RBs) < 5, flexibility for radiolabeling with carbon-11 ($t_{1/2}$ = 20.3 min) or fluorine-18 ($t_{1/2}$ = 109.8 min)) and pharmacological parameters (low nano or picomolar affinity, B_{max}/K_D > 10, > 30-100-fold target(s) selectivity).[28, 33-35]

We applied those principles in our selection process for radiotracer development from a recently reported library of 6-(2-(3-fluorophenyl)pyrrolidin-1-yl)imidazo[1,2-*b*]pyridazine pan-Trk inhibitors.[36] The validation of [^{11}C]-(*R*)-**3** as a potential clinical radiotracer emerged from the preclinical validation of a series of racemic radiolabeled derivatives with picomolar potencies for TrkB/C which included [^{11}C]-(±)-**3** (**Figure 1**, **Figure S1**). A concomitant comparative advanced preclinical evaluation of the radiolabeled pan-Trk inhibitor [^{11}C]**5** ([^{11}C]GW441756) (**Figure 1**)[37] is provided. Following preclinical validation in rodents and non-human primates (*vide infra*), radiotracer [^{11}C]-(±)-**3** was selected for structural refinement and the enantioselective synthesis of the putatively fitting *R*-enantiomer was undertaken (**Scheme 1**, **Figure 2a,b**).[36, 38] The key (*R*)-2-(3-fluorophenyl)pyrrolidine ((*R*)-**11**) intermediate required for securing (*R*)-**3** was synthesized via a Ellman sulfinamide route in place of the previously described enantioselective lithiation as the key step due to the limited availability of (-)-sparteine required using the latter technique (**Scheme 1**).[39] Diastereoselective Grignard addition to γ-chloro *N*-sulfinyl aldimine (R_S)-**8**[40] delivered the diastereomer (R_S,*R*)-**9** in 72% yield as the unique addition product (structure confirmed by X-ray crystallography, **Scheme 1**). Base-promoted ring closure followed by sulfinyl group cleavage cleanly afforded pyrrolidine (*R*)-**11** on gram scale providing an efficient and mild alternative to the known and less scalable *sec*-BuLi/lithiation sequence. With

(*R*)-**11** in hand, the carboxylic acid (*R*)-**12** (ee > 99.6%; chiral SFC/MS, **Supplementary Information Section 3**) was obtained and derivatized with the required anilines for the synthesis of the non-radioactive standard and nor-precursor (*R*)-**14**.

The non-radioactive inhibitor (*R*)-**3** displays half-maximal inhibitory concentrations (IC_{50}s) of 4.0, 0.2 and 0.1 nM for human TrkA, TrkB and TrkC, respectively, in [γ-^{33}P]ATP-based enzymatic assays (**Figure 2c**). Inhibitory measurements at K_m ATP and conversion using Cheng-Prusoff analysis[41] for competitive inhibition gave inhibitory constants (K_i) values of 2.80 ± 0.16 nM, 0.050 ± 0.005 nM and 0.021 ± 0.011 nM for TrkA, TrkB and TrkC respectively (n = 3, s.d.) (~200,000-500,000-fold over K_m ATP for Trk)[42]. (*R*)-**3** therefore exhibits notable intra-Trk isoform selectivities of 56-fold for TrkB and 133-fold for TrkC with regard to TrkA. In order to evaluate the broader selectivity profile of our lead, comprehensive kinome screening on a panel of 369 human kinases was conducted at 0.2 μM cut-off (Reaction Biology Corp., full wild type kinase panel). This assay revealed that (*R*)-**3** exhibits >1000/2000-fold TrkB/C selectivity for 99% of targets tested, with only four kinases (BMX, TXK, ACK1 and ROS1) at or above their IC_{50} values for the tested concentration (**Figure 2e**, **Supplementary Information Section 5**). Aside from BMX, which was inhibited approximately at IC_{50} with (*R*)-**3** 0.2 μM, individual dose response curves were generated for TXK, ACK1 and ROS1 revealing IC_{50}s of 106 nM, 62.6 nM and 5.96 nM respectively (**Figure 2c**,**e**). (*R*)-**3** exhibits ~30- and 60-fold selectivity for TrkB and TrkC respectively versus ROS1 – the closest off-target identified. As anticipated, (*S*)-**3** displayed still acceptable TrkB/C activities albeit in the nanomolar rather than the picomolar range (**Figure S2**).[36, 38]

Overall, for the purpose of this study, the radiosynthesis of [^{11}C]-(*R*)-**3** was implemented at four distinct production sites including a Good Manufacturing Practice (GMP)-compliant automated synthesis for first-in-human PET imaging. For human PET studies, [^{11}C]-(*R*)-**3** was prepared from (*R*)-**14** using [^{11}C]CH_3I in the presence of K_2CO_3 in DMF with radiochemical

yields (RCYs) of 13.0 ± 2.0 % (s.d., decay-corrected RCYs at end-of-synthesis based upon [^{11}C]CO_2, *n* = 3, > 99% radiochemical purity), and molar activity (A_m) of 118 GBq/μmol (**Scheme 1**). Throughout the translational imaging study, the radiosynthesis of [^{11}C]-(*R*)-**3** was highly reproducible, robust and flexible to protocol adaptation (*n* > 40). In all cases, from preclinical to clinical PET, the identity of all radiotracers including [^{11}C]-(*R*)-**3**, was confirmed by non-radioactive standard co-injection using high-performance liquid chromatography (HPLC) (**Scheme 1, Supplementary Information Section 6**).

In vivo PET imaging of [^{11}C]-(R)-3 in rodent. Initial PET imaging experiments with [^{11}C]-(±)-**3** in Sprague Dawley rats as part of the racemic series screening confirmed this scaffold as a lead based on overall brain penetration, brain-to-blood ratio and stability (**Figure S3a-c**). The radioactivity uptake of [^{11}C]-(*R*)-**3** in the FVB mouse brain (wildtype mice) was rapid and peak brain uptake (SUV_{max}) of 1.33 ± 0.19 (s.d.) was reached within 1 min following intravenous injection (i.v.) (SUV, standardized uptake value - normalization for injected dose and body weight) as illustrated by the corresponding whole-brain time-activity curve (TAC) (**Figure 3f**). The radiotracer was found extensively distributed within the CNS in accordance with reported TrkB expression (**Figure 3c**,**h**).[43] Peak brain radioactivity was followed by moderate washout throughout the remainder of the 60 min scan (0.40 ± 0.02 SUV at 60 min post injection, s.d., $\Delta_{SUVmax\text{-}60min}$ = - 69%). Biodistribution imaging studies highlighted extensive liver uptake suggesting hepatobiliary clearance as the primary route of excretion (**Figure 5.2g**).

Despite similar overall brain kinetics profile, with [^{11}C]-(±)-**3** lower SUV_{max} (1.04 ± 0.12 at 0.5 min, s.d.) were reached as compared to the enantiopure radiotracer (**Figure 3a,b,e**). These results demonstrate that [^{11}C]-(*R*)-**3** readily diffuses through the blood-brain barrier (BBB) and persists moderately in the rodent brain while suggesting faster elimination of the racemate. Comparative analysis with [^{11}C]**5**, the only available pan-Trk radiotracer lead previously reported was performed (**Figure 3j**). *In vivo* PET of [^{11}C]**5** in FVB mice revealed substantial and rapid

brain penetration (SUV_{max} of 4.14 ± 0.55 at 1 min, s.d.) which was followed by prompt and extensive washout (0.14 ± 0.02 SUV at 60 min post injection, s.d., $\Delta_{SUVmax\text{-}60min}$ = -97%, **Figure 3l**) on par with previously reported data in rats.[37] Renal clearance was more prominent with [^{11}C]**5** compared to [^{11}C]-(*R*)-**3** (**Figure 3m**). With the expectation that Trk CNS binding should be associated with tracer retention in the brain to allow for eventual quantification, the kinetics of [^{11}C]**5**, in contrast to [^{11}C]-(*R*)-**3**, likely indicate limited target engagement in rodents due to rapid subsequent washout, despite extensive initial permeation of the BBB. This observation can be rationalized in part by the significantly higher potency of [^{11}C]-(*R*)-**3** compared to [^{11}C]**5** (34-46-fold potency difference for TrkB/C). Metabolite analysis revealed [^{11}C]-(*R*)-**3** to be particularly robust *in vivo*, with > 95% intact tracer 30 min post injection in mouse blood plasma (**Figure 3i**). In order to investigate potential efflux, baseline scans were then conducted in *Mdr1a/b*$^{(-/-)}$*Bcrp1*$^{(-/-)}$ knockout mice with both [^{11}C]-(±)-**3** and [^{11}C]-(*R*)-3 (as well as [^{11}C]-(±)-**4** – data presented in **Figure S5.3** and **Figure S1d-f**). Increased whole-brain uptake was observed for all tracers (**Figure 3a-f**) indicating that primary ABC transporter components P-glycoprotein (P-gp –*Mdr1a/b*) and breast cancer resistance protein (BCRP –*Bcrp1*) at the BBB play a role in elimination of the tracer from the brain in mice. In the case of **3** tracers (racemic and *R*), this effect was most pronounced with the racemate compared to the *R*-enantiomer with $SUV_{0\text{-}60min}$ (FVB)/$SUV_{0\text{-}60min}$ (*Mdr1a/b*$^{(-/-)}$*Bcrp1*$^{(-/-)}$) ratios of 0.56 for [^{11}C]-(*R*)-**3** compared to 0.39 for [^{11}C]-(±)-**3** (**Figure 3e,f**). This result was however paralleled by opposite variations in blood radioactivity which may in part explain inter-tracer variations (**Figure 3g**, **Figure S4**). Whole brain TACs displayed kinetics consistent with results obtained in FVB mice. Calcein-AM cellular assay in P-gp and BCRP overexpressing Madin-Darby Canine Kidney (MDCKII) cells and Lineweaver-Burk plot analysis confirmed (*R*)-**3** as a P-gp/BCRP substrate with moderate affinity (EC_{50} of 2.9 ± 1.3 μM and 2.23 ± 1.1μM respectively, s.d., **Figure S5**). Interestingly, while no difference was observed in the brain distribution of [^{11}C]**5** under microdosing PET imaging

conditions between FVB and *Mdr1a/b*$^{(-/-)}$*Bcrp1*$^{(-/-)}$ mice groups (**Figure 3j-l**), the calcein-AM assay outlined P-gp interaction of **5** at higher doses (EC_{50} of 79.2 ± 8.3 μM, s.d.) (**Figure S5e**). In contrast to (*R*)-**3**, this disparity is consistent with the possibility that **5** acts as a weak P-gp inhibitor rather than a substrate.

Supported by recent next-generation sequencing (NGS) efforts, oncogenic Trk fusions have been described in over twenty tumor types, reinforcing the view that Trk chimeric proteins are low-frequency but recurrent oncogenic drivers in human cancer[2]. Yet, concerns over neurotoxicity arising from sustained CNS Trk blockade upon treatment for peripheral conditions have been described[15-16, 44-45] Current clinical trial efforts include genomically-driven phase II trials for *NTRK* fusion-positive patient subpopulations based on promising phase I results with entrectinib (**Figure 3n**, **Figure 1** and **Table S1**).[46-47] In order to provide unambiguous evidence for TrkB/C specific binding, we conducted Trk receptor heterologous blocking through pharmacological challenge *in vivo* using this inhibitor. [^{11}C]-(*R*)-**3** brain uptake following entrectinib administration (30 min intraperitoneal predosing) was investigated, simultaneously providing confirmation of brain penetration and target engagement of a currently advanced pan-Trk inhibitor clinical lead using a non-invasive technique. Pretreatment doses were selected under and above a threshold of 240 mg/kg which was previously shown to achieve 0.43 brain-to-plasma ratio in mice with sustained treatment regimen (240 mg/kg/day in continuous 2 weeks administration).[25] We observed dose-dependent whole brain radioactivity reduction ($SUV_{0\text{-}60min}$) of -7% and -40% with 50 mg/kg and 350 mg/kg pretreated mice (single doses) compared to vehicle-treated control respectively (**Figure 3o-r**). At the time of SUV_{max} (1 min post injection) in the vehicle-treated animals, brain concentration was reduced in animals treated with entrectinib at pharmacological doses (50 and 350 mg/kg respectively) by 29% and 88% respectively. This is consistent with a rapid brain penetration and target binding followed by a tracer washout. As expected, trends in brain-to-blood K_p ratios during dynamic scanning did not differ from SUV

measurements as entrectinib pretreatment did not affect blood radioactivity upon [^{11}C]-(*R*)-**3** injection (as measured at 50 mg/kg). Data from a Calcein-AM cellular assay with MDCKII cells included herein also demonstrate that entrectinib is not a prominent substrate for P-gp or BCRP (**Figure S5f**-**h**). At this point, [^{11}C]-(*R*)-**3** emerged as a unique lead on the basis of favorable pharmacology and imaging properties in FVB mice. In spite of its efflux liability at microdoses described in *Mdr1a/b*$^{(-/-)}$*Bcrp1*$^{(-/-)}$ mice, the choice of [^{11}C]-(*R*)-**3** was supported by documented inter-species variation in intracerebral disposition of actively effluxed PET tracers between rodents and higher species which was in line with our concurrently collected data in non-human primates (*vide infra*).[33, 48-49]

Evaluation of [^{11}C]-(R)-3 in the non-human primate brain. Radioactivity brain uptake following [^{11}C]-(*R*)-**3** administration was higher in non-human primates compared to rodents and displayed distinctively slow brain kinetics characterized by steady radioactivity increase without washout from brain tissue for the entire duration of the 60 min scan (**Figure 4a**, **Figure S6e**). Based on volumetric region of interest (ROI) analysis, the uptake was shown to be heterogeneously distributed, ubiquitous across gray matter regions and most pronounced in the thalamus (~0.8 SUV at 60 min post injection) while white matter displayed comparatively low accumulation (~0.3 SUV at 60 min post injection) matching known TrkB/C receptor distribution (thalamus ≥ cerebellum ≥ cortex >>> white matter) (**Figure 4a**, **Figure S6e**). Binding kinetics of [^{11}C]-(*R*)-**3** were different from [^{11}C]-(±)-**3**, exhibiting higher gray matter uptake compared to the racemic tracer 60 min post injection (**Figure 4b**, **Figure S6d**,**e**). [^{11}C]-(*R*)-**3** also presented significantly higher test-retest reproducibility of SUVs compared to [^{11}C]-(±)-**3**. Brain pharmacokinetics of [^{11}C]**5** contrasted with [^{11}C]-(*R*)-**3**, reaching SUV_{max} of 2.41 SUV in cerebellum at 4 min post injection (2.17 SUV in thalamus at 2.5 min) followed by sustained washout (**Figure 4c** and **Figure S6f**). Whole brain washout in primates was however reduced compared to mice (0.62 SUV at 60 min post injection, $\Delta_{SUVmax\text{-}60min}$ = -65%). [^{11}C]**5** and [^{11}C]-(*R*)-

3 showed identical brain concentration 60 min post injection despite opposite kinetic trends. Based on known CNS TrkB/C full length levels, regional gray-to-white matter SUV ratios ($SUV_{gray\ matter}/SUV_{white\ matter}$) were used as an estimate for specific binding and tracer prioritization. As illustrated in **Figure 4d**, specific signal approximations using summed SUV ratios for 30-60 min post injection were markedly higher for [^{11}C]-(*R*)-**3** compared to [^{11}C]-(±)-**3** and [^{11}C]**5** in all gray matter regions with representative average values of 2.3 and 2.1 in the thalamus and cerebellum respectively (similar trends were observed in 0-60 min summed data, **Figure S7**). Despite [^{11}C]**5** displaying higher uptake than [^{11}C]-(*R*)-**3**, the use of this tracer is impeded by lower specific binding, inferior target selectivity and intrinsic contamination with an inseparable [^{11}C]-(*E*)-**5** inactive photoisomer,[37] which constitute major hurdles to clinical translation. Taken together, the results obtained with [^{11}C]-(*R*)-**3** in primates are in contrast to the efflux kinetic profile in rodents and are indicative of a moderate and continuous brain uptake as well as favorable TrkB/C specific signal properties in the primate brain.

[^{11}C]-(R)-3 binding in human post-mortem brain tissue. To further assess the binding specificity and selectivity of our lead radiotracer in brain tissue as well as to provide proof-of-principle evidence of its potential use in the context of neurodegenerative diseases, *in vitro* autoradiography experiments using post-mortem tissue from human healthy control (HC) and aged-matched AD patient groups were conducted. Binding properties of [^{11}C]-(*R*)-**3** were measured in four brain regions (20 μM cryosections) including the hippocampus which has been shown to undergo drastic TrkB full length reduction in AD brains[13-14] as well as unaffected regions with regards to TrkB expression (e.g. parietal cortex and cerebellum).[50] In an initial series of baseline experiments using HC human brains (n = 12-15), [^{11}C]-(*R*)-**3** displayed extensive, yet heterogeneous total binding in all regions mirroring the near-ubiquitous expression of TrkB/C in neurons of the mammalian brain as characterized using [^{125}I]BDNF, [^{125}I]NT-3 and [^{125}I]NT-4/5 and mRNA hybridization (**Figure 5** and **Figure S8**).[43] In order to

evaluate the extent of specific binding (impact of brain lipids and proteins non-specific binding) and TrkB/C selectivity (impact of off-target receptor-mediated interactions), competition blocking experiments using the chemically distinct selective pan-Trk type I inhibitor **5** (10 μM) were conducted in HC brains. Heterologous blocking was prominent in all analyzed ROIs ($P \leq 0.0001$) with the most pronounced effects observed in the prefrontal cortex (Δ ~ -71%, n = 15) and hippocampus (Δ ~ -69%, n = 12), while significant albeit less pronounced blocking was observed in the inferior parietal cortex (Δ ~ -43%, n = 15) and cerebellum (Δ ~ -54%, n = 15), revealing high specific and TrkB/C-selective binding of [^{11}C]-(*R*)-**3** throughout the brain (**Figure 5**). Total or specific/selective binding inter-individual variability did not correlate with gender, age or post-mortem delay in HC samples. Having demonstrated excellent TrkB/C-binding in human healthy brains, measurements of total and specific/selective binding of [^{11}C]-(*R*)-**3** in post-mortem tissue from AD patients in the corresponding ROIs (n = 11-12) were performed. Total tracer binding and specific/selective-TrkB/C binding were found to be significantly reduced in the hippocampus of AD brains compared to HC (Δ ~ -35%, $P \leq 0.001$) as reported using IHC and ISH techniques.[13-14] With the exception of this effect, non-specific/non-selective levels upon blocking with 5 in AD brains were similar to the observations from HC brains suggesting strong TrkB/C interaction in the AD group as well ($P \leq 0.0001$). No additional noticeable differences between AD and HC groups in total tracer binding or specific/selective binding were observed in the other regions analyzed. Again, inter-individual binding differences within the AD brain samples could not be ascribed to differences in gender, age or post-mortem delay.

Imaging TrkB/C in the human brain using [^{11}C]-(R)-3. These preclinical data prompted the evaluation of [^{11}C]-(*R*)-**3** as a radiotracer for use in humans *in vivo*. First-in-human brain uptake measurements of [^{11}C]-(*R*)-**3** were performed in one healthy male volunteer (41 years of age). Radiotracer brain uptake was prompt with SUV_{max} reached in all analyzed ROIs at 25 sec post injection (including white matter) (1.5 SUV in the thalamus) followed by rapid stabilization and

steady retention with negligible decrease during the 60 min scan. The uptake was heterogeneous but prevalent within the gray matter regions with the highest uptake seen in the thalamus (0.7 SUV) and lowest in white matter (0.4 SUV) with overall distribution aligning with non-human primate results and known TrkB/C expression (thalamus ≥ cerebellum ≥ cortex >>> white matter) (**Figure S9a** and **Figure 6**).Uptake in gray matter regions was superior to white matter at all time points. There were no adverse events or clinically detectable pharmacologic effects associated with the injection of [^{11}C]-(*R*)-**3**.

DISCUSSION

The development of the first lead radiotracer for non-invasive PET imaging of TrkB/C receptors in the living brain and post-mortem tissue is described. Human PET imaging with [^{11}C]-(*R*)-**3** was translated from preclinical research and demonstrated moderate brain uptake in agreement with regional TrkB/C distribution and favorable gray-to-white matter ratios. It was shown that most obstacles commonly associated with the development of orthosteric probes for intracellular *in vivo* neuroimaging of protein kinases such as i) the combination of favorable physicochemical properties for rapid membrane diffusion (see result section), ii) the achievement of adequate affinity in light of high intracellular ATP concentration (hence low available receptor density, B_{avail}), as well as iii) the realization of sufficient target selectivity within the human protein kinome which presents highly conserved ATP/inhibitor-binding site can be overcome by thorough SAR screening. Our biochemical examination showed that (*R*)-**3** displays intrinsic affinity in the low picomolar range for TrkB/C. Moreover, we demonstrated that (*R*)-**3** displays exceptional kinome selectivity in comprehensive screenings (including notably TrkA) well beyond the 30-100-fold threshold considered necessary for CNS radiotracers.[28, 33] Importantly, as *in vivo* selectivity depends both on the affinity of the probe and the target density (B_{max}), the low TrkA expression compared to TrkB/C in the mammalian CNS combined with the 50-100-fold selectivity in favor of TrkB/C against TrkA infer that [^{11}C]-(*R*)-**3** *in vivo* binding should be highly restricted to TrkB/C without detectable contribution from TrkA receptor binding as intended.[43, 51] Similar, unwanted interaction with ROS1, the only target for which (*R*)-**3** shows less than 100-fold selectivity identified to date, is not an impediment foreseen due to the lack of detectable *ROS1* levels in normal human brain tissue.[52] Based on available data, (*R*)-**3** displays both the highest affinity for TrkB/C and the best kinome selectivity of all pan-Trk inhibitors characterized to date and therefore constitutes a prime lead for radiotracer development.

A central objective of the present report is to provide the most comprehensive overview of the development of [^{11}C]-(*R*)-**3** from radiotracer design to human use. At its core, the work presented here was enabled by the efficient enantioselective synthesis of the required non-radioactive standard and nor-precursor as well as by the reliable radiosynthesis of [^{11}C]-(*R*)-**3**. In particular, we showed that [^{11}C]-(*R*)-**3** can be obtained in high molar activity, excellent radiochemical purity as well as sufficient isolated RCYs both in manual radiosyntheses as well as in fully GMP-compliant automated radiosyntheses for use in clinical studies. In addition, with extensive metabolism often emerging as a detrimental factor precluding radiotracer development, we investigated the stability of [^{11}C]-(*R*)-**3** *in vivo*. Only < 5% of emerging polar metabolites were detected during *in vivo* radio-TLC metabolism studies. No lipophilic metabolites that could pass the BBB were observed. Our report also highlights the importance of multi-tracer/multi-species translational studies in the context of PET radiotracer development.

To provide additional evidence of TrkB/C specificity and selectivity of [^{11}C]-(*R*)-**3** in brain tissue, we determined radiotracer binding properties in autoradiography experiments using healthy human brain tissue. In a first set of data collected using HC tissue, we showed extensive specific and selective binding, using the selective pan-Trk inhibitor **5** as a second structurally distinct heterologous pharmacological competitor. Anomalies in neurotrophin/Trk receptor systems have been described in various CNS diseases and conditions and are best characterised in the context of AD. For instance, genome association analysis has suggested a possible role for polymorphism of the genes for both *BDNF* and *NTRK2* (TrkB) as risk factors in AD,[53] although this remains a subject of debate.[54] Direct evidence of involvement of the BDNF/TrkB system in AD comes from studies indicating that TrkB full length levels are profoundly decreased in the hippocampus of patients with AD,[13] although apparently not in the parietal cortex.[50] Moreover, progressive loss of TrkB signal (as well as of the TrkA/C variants) in basal forebrain cholinergic nuclei is well correlated with the clinical progression of the disease.[11]

Treatment with agonists of the BDNF/TrkB system in transgenic mice models of AD results in an increase of dendritic spines in the hippocampus and cortex, an inhibition of neuronal apoptosis and neurodegeneration, and improves spatial memory performance.[55-57] We therefore used AD as a proof-of-concept for the application of [^{11}C]-(*R*)-**3** as quantitative radiotracer, and determined a [^{11}C]-(*R*)-**3** specific binding profile in AD brains as a parallel study to our HC experiments. Considering known trends previously measured using IHC, we show that hippocampal [^{11}C]-(*R*)-**3** binding is significantly decreased in AD versus HC. Those results indicate the potential use for Trk PET radiotracers in the study and diagnosis of neurodegenerative diseases. While our study design did not allow for pharmacological blocking in non-human primates due to the lack of an approved Trk inhibitor (ideally also BBB permeable) or other suitable tool inhibitors with prominent Trk activity and established safety profile, multiple lines of evidence are provided illustrating a displaceable specific binding of [^{11}C]-(*R*)-**3** both *in vitro* and *in vivo* together with concordant regional CNS distributions in the human and non-human primate brain. We recognize that the absolute brain uptake of our lead radiotracer is moderate which imply that further structural optimization will be required to reach optimal clinical utility. The absence of a gold-standard radiotracer for comparison however precludes the determination of what constitutes a standard brain uptake in this context. Currently, the only other radiolabeled kinase inhibitor shown to engage its target *in vivo* is the glycogen synthase kinase-3 (GSK3) tracer [^{11}C]PF-367.[58] Notably, in a preclinical non-human primate study, this tracer displayed brain uptake comparable to [^{11}C]-(*R*)-**3** while not being susceptible to P-gp efflux. It is, at the moment, not possible to discern whether the observed brain disposition of [^{11}C]-(*R*)-**3** in higher species is primarily related to active efflux transport or other factors such as TrkB/C.FL B_{max} which has not been defined in human tissue yet.

CONCLUSION

In summary, our study provides a molecular imaging tool tracer for the *in vitro* and *in vivo* non-invasive study of neuronal signal transduction at the interface of neurology and oncology which is as of yet unexplored. Importantly, the data described herein delineates, to the best of our knowledge, the first use of a small molecule kinase inhibitor radiotracer as an *in vivo* probe to explore endogenous kinase densities using PET neuroimaging in human. Using port-mortem tissue, it is anticipated that our molecular probe should provide a rapid mean to clarify TrkB/C expression levels in a wide range of neurological diseases wherein TrkB/C dysregulation has long been suspected to play a prominent pathogenic role. In particular, when taking into account the intrinsic *in vivo* translatability of our approach, the finding that the primary radiotracer identified herein enables the discrimination of AD from HC brains could ultimately have substantial implications for AD diagnostic beyond conventionally sought biomarkers. Given also that the primary safety concern in the current efforts towards the development of Trk TKIs as novel antineoplastic and antinociceptive drug classes remain the prospect of unwanted CNS neurotoxicity via TrkB/C inhibition, our approach provides an immediate tool to screen CNS occupancy non-invasively in preclinical settings as shown for entrectinib here.[45, 59-60] Our efforts currently revolve around conducting iterative structural optimization in order to mitigate efflux liabilities, improve brain pharmacokinetics, and identify second generation leads based on the *(R)*-2-(3-fluorophenyl)pyrrolidin-1-yl)imidazo[1,2-*b*]pyridazine scaffold to clarify the exact determinants presiding to the observed brain uptake of in human and non-human primates.

EXPERIMENTAL SECTION

General Methods for Chemistry. All moisture sensitive reactions were carried out in oven-dried flasks under nitrogen atmosphere with dry solvents. Reagents and solvents were purchased at the highest commercial quality from Fisher, Sigma-Aldrich, Alfa-Aesar, Synthonix or Oakwood Products and were used without further purification unless specified otherwise. Compounds used for blocking PET studies, **5** hydrochloride and entrectinib, were purchased from Aldrich (G3420) and Cedarlane (HY-1267) respectively. Organic solutions were concentrated under reduced pressure on a Heidolph rotary evaporator. In general, reactions were magnetically stirred and monitored by TLC performed on pre-coated glass-backed TLC plates (Analtech, 250 microns) and chromatographic purification of products was accomplished using flash chromatography on Alfa-Aesar silica gel (230-450 mesh). TLC visualization was performed by fluorescence quenching, $KMnO_4$ or ninhydrin. ^{1}H NMR and ^{13}C NMR spectra were recorded on a Agilent/Varian DD2 MR two channel 400 MHz spectrometer, a Agilent/Varian VNMRS two-channel 500 MHz spectrometer or a Agilent/Varian Inova four-channel 500 MHz spectrometer in $CDCl_3$ or d_6-DMSO and peak positions are given in parts per million using TMS as internal standard. Peaks are reported as: s = singlet, d = doublet, t = triplet, q = quartet, p = quintet, m = multiplet, b = broad; coupling constant(s) in Hz; integration. High Resolution Mass Spectra (HRMS) analysis was obtained from the Mass Spectrometry Facility of the Chemistry Department of the University of Alberta (Agilent Technologies 6220 oaTOF) or from the Regional Center for Mass Spectrometry of The Chemistry Department of the Université de Montréal (LC-MSD-TOF Agilent). Compounds tested for biological evaluation were >95% pure (HPLC). The chiral SFC/MS analysis was performed at the Regional Mass Spectrometry Center of the department of chemistry of the Université de Montréal. Crystallographic analysis was performed by the X-Ray Diffraction Laboratory of the department of chemistry of the Université de Montréal.

The syntheses of (±)-**15**, (±)-**4** ((±)-IPMICF22), (±)-**2** ((±)-IPMICF10), (±)-**1** ((±)-IPMICF6), (±)-**3** and (±)-**12** (**Figure S2**) have been reported in the literature.[36] The synthetic sequences leading to the radiolabeling precursors (±)-**14** and (*R*)-**14** as well as the compounds (*R*)-**3**/(*S*)-**3** are described here. The synthesis of compound (R_S)-**8** has been described in the literature.[40] The absolute stereochemistry of (R_S,*R*)-**9** was confirmed by X-ray crystallography analysis. Compounds (*R*)-**12,** (*R*)-**13**), (*R*)-**14** and (*R*)-**3** were synthesized in accordance with the methods described for the corresponding racemic compounds. All R_f/NMR/MS data obtained for those compounds were in full agreement with the corresponding known racemates. The synthesis of (*S*)-**3** was carried out following the procedure described for (*R*)-**3** with (S_S)-**8** as starting material. The synthesis of compound (S_S)-**8** has been described in the literature[3]. All R_f/NMR/MS data obtained for compounds (S_S,*S*)-**9** and (S_S,*S*)-**10** were in full agreement with the corresponding (R_S,*R*)-enantiomers. The enantiopurities of the pyrrolidine C2 centers in both the (*R*)- and (*S*)-synthetic sequences were further confirmed at the stage of the key intermediates (*R*)-**12** and (*S*)-**12** using chiral SFC/MS analysis (ee > 99.6%). ^{1}H and ^{13}C spectra of new compounds and chiral SFC analysis are provided in *SI* Appendix.

Chemistry.

4-((tert-Butyldimethylsilyl)oxy)-3-fluoroaniline (**17**). *tert*-Butyldimethylsilyl chloride (791 mg, 5.25 mmol, 1.05 equiv) was added to a solution of 4-amino-2-fluorophenol (636 mg, 5.0 mmol, 1.0 equiv) and imidazole (851 mg, 12.5 mmol, 2.5 equiv) in anhydrous acetonitrile (25 mL) at 23°C. The reaction mixture was stirred at this temperature for 12 h and then diluted with water (50 mL) and ethyl acetate (50 mL). The organic layer was separated and extracted with ethyl acetate (3 X 50 mL). The organic layers were combined, washed with brine (50 mL) and dried over anhydrous sodium sulfate, filtered and concentrated under reduced pressure. The crude product was purified by flash column chromatography (25→50% ethyl acetate in hexane) to afford 712 mg of the title compound (59%). Physical State: red oil. R_f: 0.57 (1:1 hexanes/EtOAc, UV light).

HRMS (ESI+): *m/z* calc. for $C_{12}H_{21}FNOSi$ $(M + H)^+$: 242.1371, found 242.1368. ^{1}H NMR (400 MHz, CHLOROFORM-*d*): δ = 6.71 (dd, *J* = 8.6, 9.3 Hz, 1H), 6.42 (dd, *J* = 2.8, 12.1 Hz, 1H), 6.31 (ddd, *J* = 1.3, 2.8, 8.5 Hz, 1H), 3.61 - 3.30 (m, 2H), 1.04 - 0.94 (m, 9H), 0.15 (d, *J* = 1.0 Hz, 6H). ^{13}C NMR (101 MHz, CHLOROFORM-*d*): δ =154.4 (d, *J* = 242.8 Hz, 1C), 141.1 (d, *J* = 9.1 Hz, 1C), 135.3 (d, *J* = 12.6 Hz, 1C), 122.7 (br d, *J* = 3.1 Hz, 1C), 110.7 (d, *J* = 3.1 Hz, 1C), 103.9 (br d, *J* = 22.2 Hz, 1C), 25.6, 18.2, -4.8 (br d, *J* = 1.7 Hz, 1C).

N-(4-((tert-Butyldimethylsilyl)oxy)-3-fluorophenyl)-6-(2-(3-fluorophenyl)pyrrolidin-1-yl)imidazo[1,2-b]pyridazine-3-carboxamide ((±)-(**13**). *N,N*-Diisopropylethylamine (0.12 mL, 0.69 mmol, 2.5 equiv) was added to a solution of 6-(2-(3-fluorophenyl)pyrrolidin-1-yl)imidazo[1,2-*b*]pyridazine-3-carboxylic acid ((±)-**12**, 90 mg, 0.28 mmol, 1.0 equiv) in *N,N*-dimethylformamide (3 mL). HATU (107 mg, 0.28 mmol, 1.0 equiv) was then added in one portion and the reaction mixture was stirred at 23°C for 5 min. A solution of 4-((*tert*-butyldimethylsilyl)oxy)-3-fluoroaniline (**17**) 81 mg. 0.34 mmol, 1.2 equiv) in *N,N*-dimethylformamide (1 mL) was added dropwise and the reaction mixture was stirred at 23°C for 12 h. The reaction mixture was diluted with ethyl acetate (50 mL), washed with water (25 mL) and brine (25 mL), dried over anhydrous sodium sulfate, filtered and concentrated under reduced pressure. The crude product was purified by flash column chromatography (1→5% methanol in dichloromethane) to afford 96 mg of the title compound (62%). Physical State: white solid. R_f: 0.13 (1:99 MeOH/CH_2Cl_2, UV light). HRMS (ESI+): *m/z* calc. for $C_{29}H_{34}F_2N_5O_2Si$ $(M + H)^+$: 550.2444, found 550.2458. ^{1}H NMR (498 MHz, CHLOROFORM-*d*): δ = 10.46 (br s, 1H), 8.29 (s, 1H), 7.72 (br d, *J* = 9.9 Hz, 1H), 7.51 (br s, 1H), 7.34 - 7.29 (m, 1H), 7.05 - 6.95 (m, 3H), 6.93 - 6.86 (m, 2H), 6.60 - 6.53 (m, 1H), 5.11 (br d, *J* = 7.9 Hz, 1H), 4.03 - 3.95 (m, 1H), 3.84 - 3.76 (m, 1H), 2.63 - 2.54 (m, 1H), 2.23 - 2.10 (m, 3H), 1.04 (s, 9H), 0.23 (s, 6H). ^{13}C NMR (125 MHz, CHLOROFORM-*d*): δ = 163.2 (d, *J* = 247.5 Hz, 1C), 157.0, 153.8 (br d, *J* = 244.1 Hz, 1C), 152.1, 145.1 - 144.9 (m, 1C), 144.8 - 144.6 (m,

1C), 139.8 (d, *J* = 12.6 Hz, 1C), 138.0, 132.0 (br s, 1C), 130.7 (br d, *J* = 8.3 Hz, 1C), 127.2, 122.1, 121.1 (br d, *J* = 2.6 Hz, 1C), 116.1 (br s, 1C), 115.9 - 115.7 (m, 1C), 114.6 (br d, *J* = 21.4 Hz, 1C), 112.6 (br d, *J* = 22.2 Hz, 1C), 110.9 (br s, 1C), 109.4 (br s, 1C), 62.1, 48.7, 35.9, 25.6, 22.8, 18.3, -4.7.

N-(3-Fluoro-4-hydroxyphenyl)-6-(2-(3-fluorophenyl)pyrrolidin-1-yl)imidazo[1,2-b]pyridazine-3-carboxamide ((±)-(**14**). Tetrabutylammonium fluoride (1.0 M in tetrahydrofuran, 0.23 mL, 0.23 mmol, 1.5 equiv) was added dropwise to a solution of *N*-(4-((*tert*-butyldimethylsilyl)oxy)-3-fluorophenyl)-6-(2-(3-fluorophenyl)pyrrolidin-1-yl)imidazo[1,2-*b*]pyridazine-3-carboxamide ((±)-**7**, 85 mg, 0.15 mmol, 1.0 equiv) in tetrahydrofuran (5 mL) at 23°C. After 2 h, the reaction mixture was quenched with water (25 mL) and diluted with ethyl acetate (50 mL). The organic layer was separated and the aqueous layer was washed with ethyl acetate (3 X 50 mL). The organic layers were combined, washed with brine (50 mL) and dried over anhydrous sodium sulfate, filtered and concentrated under reduced pressure. The crude product was purified by flash column chromatography (1→10% methanol in dichloromethane) to afford 65 mg of the title compound (91%). Physical State: tan solid. R_f: 0.45 (1:9 MeOH/CH_2Cl_2, UV light). HRMS (ESI+): *m/z* calc. for $C_{23}H_{20}F_2N_5O_2$ $(M + H)^+$: 436.1580, found 436.1596. ^{1}H NMR (400 MHz, DMSO-d_6): δ = 7.98 (s, 1H), 7.77 (d, *J* = 9.9 Hz, 1H), 7.42 (br dd, *J* = 1.9, 12.9 Hz, 1H), 7.27 - 7.16 (m, 1H), 7.01 (d, *J* = 7.8 Hz, 1H), 6.96 (td, *J* = 1.9, 10.0 Hz, 1H), 6.92 - 6.83 (m, 3H), 6.80 (d, *J* = 10.0 Hz, 1H), 5.19 (dd, *J* = 1.5, 8.0 Hz, 1H), 4.01 - 3.90 (m, 1H), 3.76 - 3.65 (m, 1H), 2.07 - 1.88 (m, 3H), 1.59 - 1.48 (m, 1H). ^{13}C NMR (101 MHz, DMSO-d_6): δ = 163.0 (d, *J* = 245.0 Hz, 1C), 156.8, 152.6, 150.9 (d, *J* = 240.0 Hz, 1C), 145.9 (d, *J* = 6.2 Hz, 1C), 141.7 (d, *J* = 12.5 Hz, 1C), 136.6, 130.6 (d, *J* = 8.3 Hz, 1C), 129.9 (d, *J* = 9.1 Hz, 1C), 126.6, 124.7, 122.1, 121.7 (d, *J* = 2.7 Hz, 1C), 117.9 (d, *J* = 3.3 Hz, 1C), 117.0 (br s, 1C), 113.9 (d, *J* = 21.4 Hz, 1C), 112.8, 112.5 (br d, *J* = 8.3 Hz, 1C), 109.7, 61.8, 48.6, 35.6, 22.6.

(R)-N-((R)-4-Chloro-1-(3-fluorophenyl)butyl)-2-methylpropane-2-sulfinamide ((*R*$_S$,*R*)-(**9**). To a solution of (*R*$_S$)-**8** (900 mg, 4.29 mmol, 1.0 equiv) in CH_2Cl_2 (22 mL) at -78 °C under nitrogen was added 3-fluorophenylmagnesium bromide (5.15 mL of 1.0 M THF solution, 5.15 mmol, 1.2 equiv). The reaction mixture was stirred at -78 °C for 4 h, brought to room temperature and quenched with saturated NH_4Cl (25 mL). The organic layer was washed with saturated $NaHCO_3$ (25 mL), brine (25 mL), dried over anhydrous sodium sulfate, filtered and concentrated under reduced pressure. The crude product was purified by flash column chromatography (20→100% ethyl acetate in hexane) to afford 942 mg of the title compound (72%). For X-ray crystallography analysis, the title compound was recrystallized from EtOAc/hexanes yielding white needles. Physical State: White solid. R_f: 0.17 (1:4 EtOAc/hexanes, UV light/$KMnO_4$). HRMS (ESI+): *m/z* calc. for $C_{14}H_{22}ClFNOS$ $(M + H)^+$: 306.1089, found 306.1084. ^{1}H NMR (498 MHz, CHLOROFORM-*d*) δ = 7.32 (dt, *J* = 5.9, 7.9 Hz, 1H), 7.11 (d, *J* = 7.7 Hz, 1H), 7.04 (td, *J* = 2.1, 9.7 Hz, 1H), 7.01 - 6.97 (m, 1H), 4.40 - 4.34 (m, 1H), 3.49 (t, *J* = 6.5 Hz, 2H), 3.45 (d, *J* = 3.9 Hz, 1H), 2.19 - 2.09 (m, 1H), 1.95 - 1.85 (m, 1H), 1.82 - 1.71 (m, 1H), 1.67 - 1.57 (m, 1H), 1.23 (s, 9H). ^{13}C NMR (125 MHz, CHLOROFORM-*d*) δ = 163.0 (d, *J* = 247.0 Hz, 1C), 144.6 (d, *J* = 6.7 Hz, 1C), 130.4 (br d, *J* = 8.3 Hz, 1C), 122.9 (br d, *J* = 2.8 Hz, 1C), 115.0 (d, *J* = 21.2 Hz, 1C), 113.9 (d, *J* = 21.9 Hz, 1C), 58.1, 55.9, 44.5, 33.9, 28.7, 22.6.

(R)-1-((R)-tert-Butylsulfinyl)-2-(3-fluorophenyl)pyrrolidine ((*R*$_S$,*R*)-(**10**). To a solution of (*R*$_S$,*R*)-**9** (3.25 g, 11.9 mmol, 1.0 equiv) in THF (50 mL) at 23°C was added LiHMDS (17.9 mL of 1.0 M THF solution, 17.9 mmol, 1.5 equiv). The reaction mixture was stirred at 23°C for 1 h and quenched with NH_4Cl (25 mL) and extracted ethyl acetate (3 X 50 mL). The organic layers were combined, washed with brine (50 mL) and dried over anhydrous sodium sulfate, filtered and concentrated under reduced pressure. The crude product was purified by flash column chromatography (20→40% ethyl acetate in hexane) to afford 2.29 g of the title compound

(71%). Physical State: white solid. R_f: 0.38 (2:3 EtOAc/hexanes, UV light). HRMS (ESI+): *m/z* calc. for $C_{14}H_{22}FNOS$ $(M + H)^+$: 270.1328, found 270.1322. ^{1}H NMR (498 MHz, CHLOROFORM-*d*) δ = 7.27 (dt, *J* = 6.0, 7.9 Hz, 1H), 7.03 (td, *J* = 0.7, 7.7 Hz, 1H), 6.96 (td, *J* = 2.1, 10.0 Hz, 1H), 6.93 - 6.87 (m, 1H), 5.07 (dd, *J* = 2.8, 8.2 Hz, 1H), 3.68 - 3.61 (m, 1H), 3.60 - 3.53 (m, 1H), 2.21 - 2.12 (m, 1H), 1.94 - 1.86 (m, 1H), 1.85 - 1.78 (m, 1H), 1.77 - 1.71 (m, 1H), 1.06 (s, 9H). ^{13}C NMR (125 MHz, CHLOROFORM-*d*) δ = 162.9 (d, *J* = 245.9 Hz, 1C), 147.6 (d, *J* = 6.5 Hz, 1C), 129.9 (d, *J* = 8.3 Hz, 1C), 122.1 (br d, *J* = 2.8 Hz, 1C), 113.5 (br d, *J* 5 .9 Hz, 1C), 113.3 (br d, *J* = 6.7 Hz, 1C), 57.5, 56.8, 55.2, 36.5, 24.2, 23.0.

(R)-2-(3-fluorophenyl)pyrrolidine ((*R*)-(**11**). To a solution of (*R*)-**10** (660 mg, 2.45 mmol, 1.0 equiv) in MeOH (10 mL) was added HCl (2.0 mL, 4.0 M solution in dioxane). The reaction mixture was stirred 45 min at 23°C and then concentrated to dryness. The crude residue was dissolved in water (10 mL) and neutralized to pH ~ 12 using a 6 N NaOH solution. The aqueous phase was extracted with ethyl acetate (5 X 10 mL). The organic layers were combined, washed with brine (50 mL) and dried over anhydrous sodium sulfate, filtered and concentrated under reduced pressure to afford 400 mg of the crude title compound (99%, crude) which was used directly in the following step without further purification.

In Vitro Biological Evaluations. The potencies of (*R*)-**3** and (*S*)-**3** and the K_i values and selectivity profile (369 kinases) for (*R*)-**3** were obtained through [γ-^{33}P]ATP-based enzymatic assays (Reaction Biology Corporation, Malvern, PA). Complete description of the assays can be found in the *SI* Appendix (**Supplementary Information Section 6**).

Docking analyses. Molecular docking simulations of (*R*)-**3** were performed using the X-ray co-crystal structure of the TrkB-cpdn5 complex (PDB code: 4AT3), the TrkA-*N*4-(4-

morpholinophenyl)-*N*6-(pyridin-3-ylmethyl)pyrido-[3,2-*d*]pyrimidine-4,6-diamine complex (PDB code: 4PMT) using the FITTED 3.5 program (FORECASTER platform). Docking structures and figures were prepared using Pymol.

P-gp/BCRP Assays and Lineweaver-Burk plot analysis. *Cell Culture.* Native MDCKII cells or stably transfected with human P-gp or wild-type BCRP (482A) were seeded at a density of 156.250 cells/cm^2 using Dulbecco's modified Eagle's medium (DMEM) with 10% FCS, 4.0 mM L-Glutamine, 100 U/ml Penicillin, 100 µg/ml Streptomycin and 100 µg/ml Kanamycin (Biochrom, Munich, Germany) and split after reaching cell confluency to 70-80%. Cell passages from 7-25 have been used throughout the experiments. *Calcein-AM Uptake-Assay.* The assay for quantifying P-gp efflux activity was performed as described previously.[61] Briefly, human P-gp overexpressing MDCKII cells were washed two times with Krebs-Ringer Buffer (142 mM NaCl, 3 mM KCl, 1.5 mM K_2HPO_4*3 H_2O, 10 mM HEPES, 4 mM D-Glucose, 1.2 mM $MgCl_2$, 1.4 mM $CaCl_2$, pH 7.4) and preincubated with 100 µl of double-concentrated modulator for 15 min that was followed by addition of 100 µl 4°C cold 2 µM Calcein-AM (Sigma-Aldrich, Taufkirchen, Germany) solution for 30 min. Plates were incubated at 37°C at 200 rpm. Control cells were exposed to Calcein-AM in absence of a transport modulator. Subsequently, MDCKII cells were washed with ice-cold Krebs-Ringer Buffer to stop transporter activity and intracellular fluorescence was released after incubation with 0.1% Triton X for 20 min at 37°C. The amount of intracellular fluorescence was recorded using a fluorescence plate reader (Tecan Infinite F200 Pro, $\lambda_{(excitation)}$ = 485 nm and $\lambda_{(emission)}$ = 520 nm). Background fluorescene was subtraced from each signal and intracellularly accumulated fluorescence was related to control cells. EC_{50} values were calculated via non-linear regression using the 4-parameter logistic equation with variable Hill-slope (GraphPad Prism® version 6.01) to generate dose-response curves. *Lineweaver-Burk Plot.* First, Michaelis-Menten Kinetics were calculated from efflux experiments measuring extracellular fluorescence every 90 sec on a Tecan Infinite F200 Pro. The kinetics

were determined by assigning the linear gradient of the efflux curve (RFU (relative fluorescent unit verse time) as velocity (v=RFU/time.) against the respective Calcein-AM concentration ([S]=1, 2 and 3 μM) according to the following equation:

$$\frac{v_{max} * [S]}{K_m + [S]} = v$$

where v represents the efflux velocity, v_{max} the maximum reaction velocity, [S] the Calcein-substrate concentration and K_m the Michaelis-Menten constant. A Lineweaver-Burk-Plot was obtained by plotting 1/v as the ordinate against 1/[S] as the abscissa to estimate the type of inhibitory mode. *BODIPY-Prazosin Uptake-Assay.* BCRP efflux activity was analysed in native and human Bcrp MDCKII cells employing a flow cytometer (FACSCalibur™ flow cytometer, Becton–Dickinson). In general, the net uptake of the BCRP-specific fluorescent substrate BODIPY-Prazosin into MDCKII cells in presence or absence of BCRP modulators or non-modulators was determined.[62] MDCKII cells were grown as monolayer, trypsinised and the density adjusted to 2.5×10^7 cells/ml in DMEM/Ham's F12 1:1. Hence, cells were washed twice with 37°C pre-warmed medium and increasing concentrations of test compound added to a volume of 600μl cell suspension. Cells were incubated for 15 min at 37°C and 300 μl BODIPY-Prazosin in DMEM/Ham's F12 1:1 (2 μM) was added to a final concentration of 0.5 μM and incubated for 30 min at 37°C, 700 rpm (Thermoshaker Incubator, Thriller®, Peqlab). Subsequently, the incubation was stopped with ice-cold medium and suspensions were centrifuged at 200×g for 5 min and washed with 4°C PBS (2% FCS). Finally, intracellular BODIPY-Prazosin fluorescence was measured using a FACSCalibur™ flow cytometer equipped with a 488 nm argon laser and a 530/ 30 band-pass filter. By gating on forward and sideward scatter, MDCKII cells were selected and dead cells excluded likewise using propidium iodide staining (1.0 μg/ml). Twenty thousand cells were sorted in one run. Data were analysed with CellQuest™ Pro (Franklin Lakes, NJ, USA). The increase in intracellular fluorescence (MF,

median fluorescence) caused by a test compound was referred to control fluorescence levels (100%) and given as percentage of control.

Radiochemical Syntheses. The complete descriptions of the radiochemical syntheses for preclinical studies (three sites: manual synthesis at the Edmonton PET Center (University of Alberta), automated synthesis at the McConnell Brain Imaging Center (McGill University) and automated synthesis at the University of Michigan PET Center (University of Michigan)) and first-in-human study (one site: Ludwig-Maximilians-University of Munich) are provided in *SI* Appendix (**Supplementary Information Section 6**). The manual and automated radiosyntheses of [^{11}C]-(±)-**3** and [^{11}C]-(*R*)-**3** proceeded from the desmethyl phenolic precursors and the manual and automated radiosyntheses of [^{11}C]-(±)-**4** proceeded from the corresponding primary amide as described in *SI* Appendix. The manual radiosyntheses of [^{18}F]-(±)-**1**, [^{18}F]-(±)-**2** and [^{11}C]**5** were performed as previously reported[36,38]. Briefly, for human study, [^{11}C]CO_2 was produced via the ^{14}N(p,α)^{11}C reaction by proton irradiation of a N_2/1% O_2 target of a GE PETtrace cyclotron and converted into [^{11}C]CH_3I by reduction with H_2/Ni and iodination with I_2 using a GE FX C Pro automated module. [^{11}C]CH_3I was bubbled into a solution of the precursor (*R*)-**14** (1.7 mg in 0.3 mL DMF) and K_2CO_3 (10 µL of a saturated aq. solution) at -20°C. The crude mixture was heated to 80°C for 3 min, diluted with HPLC eluent (1.5 mL,) and purified via semipreparative HPLC (Phenomenex LUNA C18 column, 100 Å, 250 × 10 mm, 10 µm, 75% MeCN/25% H_2O (v/v) isocratic; flow rate: 3 mL/min). The pure [^{11}C]-(*R*)-**3** was diluted with 10 mL H_2O, trapped on a preconditioned C18 cartridge (Waters SepPak C18 light), washed with water (3 mL) and then eluted with EtOH (1 mL) followed by sterile filtration and formulation with PBS. [^{11}C]-(*R*)-**3** was obtained in 13 ± 2 % decay-corrected radiochemical yield at end-of-synthesis based upon [^{11}C]CO_2, n = 3, radiochemical purity > 99%, S_A = 118 GBq/µmol.

Rodent PET Imaging Studies*. Animals*. All animal studies were carried out according to the guidelines of the Canadian Council on Animal Care (CCAC) and approved by the Cross Cancer

Institute Animal-Care Committee (AC14214). *In vivo* studies were done using female Sprague Dawley rats (body weight: 320-420 g, University of Alberta, Edmonton, AB, Canada, 6-12 months of age), normal female FVB mice (body weight: 24-30 g, Charles-River Laboratories, Quebec, Canada, 3-9 months of age) and female Mdr1a/b$^{(-/-)}$Bcrp1$^{(-/-)}$ mice (body weight: 24-30 g, Taconic, Hudson, NY, USA, 3-9 months of age). *Imaging procedure and analysis*. PET imaging scans of [^{18}F]-(±)-**1**, [^{18}F]-(±)-**2**, [^{11}C]-(±)-**3**, [^{11}C]-(±)-**4**, [^{11}C]-(*R*)-**3** and [^{11}C]**5** were performed on an INVEON® PET scanner (Siemens Preclinical Solutions, Knoxville, TN, U.S.A.). PET imaging experiments followed the same procedure for all 6 radiotracers: Prior to radiotracer injection, rodentswere anesthetized through inhalation of isoflurane in 40% oxygen/ 60% nitrogen (gas flow 1 L/min), and body temperature was kept constant at 37 °C. Mice or rats were placed in a prone position into the center of the field of view. A transmission scan for attenuation correction was only acquired for rat experiments, not for mice. Mice were injected with 10-50 MBq of ^{11}C-labeled radiotracer in 100-150 µL of isotonic saline solution (0.9% w/v of NaCl) through a tail vein catheter. Rats were injected with 15-72 MBq of ^{11}C-labeled or 11-21 MBq of ^{18}F-labeled radiotracer in 200-600 µL of saline solution (0.9% w/v of NaCl). Data acquisition was performed over 60 min in 3D list mode. The dynamic list mode data were sorted into sinograms with 54 time frames (10 × 2, 8 × 5, 6 × 10, 6 × 20, 8 × 60, 10 × 120, 6 × 300 s). The frames were reconstructed using maximum a posteriori (MAP) as reconstruction mode. No correction for partial volume effects was applied. The image files were processed using the ROVER v2.0.51 software (ABX GmbH, Radeberg, Germany). Masks defining 3D regions of interest (ROI) were set, and the ROIs were defined by 50% thresholding. Mean standardized uptake values [SUV_{mean} = (activity/mL tissue)/(injected activity/body weight), mL/g] were calculated for each ROI, and time−activity curves (TAC) were generated. All semi-quantified PET data are presented as means ± SD.

Metabolic Stability Study in Vivo. One normal FVB mouse was anesthetized through inhalation of isoflurane in 40% oxygen/60% nitrogen (gas flow 1 L/min) prior to intravenous injection of 117 MBq [^{11}C]-(*R*)-**3** via the tail vein. Venous blood samples were collected at 5, 15 and 30 min post injection through the tail vein catheter and further processed as follows: Blood cells were separated by centrifugation (13,000 rpm × 5 min). The supernatant was removed, and proteins were precipitated by addition of 2 volume parts of methanol (2 vol of MeOH/1 vol of sample). Another centrifugation step (13,000 rpm × 5 min) was performed to separate plasma as supernatant from the precipitated proteins. The clear plasma supernatants were analyzed by radio-TLC to determine the fraction of intact radiotracer (10%MeOH/CH_2Cl_2 R_f = 0.8).

Non-Human primates PET Imaging Studies. *Animals*. All primate imaging studies were performed in accordance with the standards set by the University Committee on Use and Care of Animals (UCUCA) at the University of Michigan. Imaging was done using a mature female rhesus monkey (*Macaca mulatta*) (body weight = 6.1 kg with negligible variation throughout the duration of the study, 15 years of age). *Imaging procedure and analysis*. PET imaging of [^{18}F]-(±)-**1**, [^{18}F]-(±)-**2**, [^{11}C]-(±)-**3**, [^{11}C]-(±)-**4**, [^{11}C]-(*R*)-**3** and [^{11}C]**5** was done using the Concorde Microsystems MicroPET P4 tomograph. PET imaging experiments followed the same procedure for all 6 radiotracers analyzed. The animal was anesthetized (isoflurane) and intubated, a venous catheter was inserted into one hindlimb and the animal positioned on the bed of the MicroPET gantry. A head-holder was used to prevent motion artifacts. Isoflurane anesthesia was continued throughout the study. Following a transmission scan, the animal was injected *i.v.* with the radiotracer (96-167 MBq) as a bolus over 1 min, and the brain imaged for 90 min (5 x 1 min frames – 2 x 2.5 min frames – 2 x 5 min frames – 7 x 10 min frames) for radiotracers or 60 min (5 x 1 min frames – 2 x 2.5 min frames – 2 x 5 min frames – 4 x 10 min frames) for ^{11}C radiotracers. Emission data were corrected for attenuation and scatter, and reconstructed using the 3D maximum a priori method (3D MAP algorithm). Using a summed image of the entire data

set, regions of interest (ROIs) were drawn manually on multiple planes to obtain volumetric ROIs for the whole brain, thalamus, cortex, pons, cerebellum and subcortical white matter. The volumetric ROIs were then applied to the full dynamic data sets to obtain the regional tissue time-radioactivity data. All semiquantified PET data are presented as means ± SD when applicable.

Human Tissue Autoradiography. Frozen brain samples from age-matched healthy controls and AD-positive brains (diagnosis confirmed by neuropathological reports; CERAD criterion) were obtained from the Douglas-Bell Canada Brain Bank (Douglas Mental Health University Institute, Montreal, Canada). Utilization of these samples was approved by both the Douglas Institute's research ethics board and the Brain Bank's scientific review committee. Samples were excluded in cases of psychiatric conditions, epilepsy, non-AD dementia, brain neoplasms, and traumatic brain injuries. In total, brain tissue from 29 subjects was analyzed (16 healthy controls and 13 AD: 23 samples from the hippocampus (HP) (12 controls, 11 AD), 27 samples from the prefrontal cortex (PFC) (15 controls, 12 AD), 27 samples from the inferior parietal cortex (IPC) (15 controls, 12 AD) and 26 samples from the cerebellum (CB) (15 controls, 11 AD) (see Table S3). Using a freezing sliding microtome (Leica CM3050S) at −15°C, each block of tissue was cut into serial 20μm-thick sections, which were then thaw-mounted on coated microscope slides. Baseline and blocking experiments were performed on adjacent sections. The optimal conditions for the *in vitro* autoradiography binding techniques such as incubation time, washing procedure, and time of exposure onto the phosphor imaging plate were obtained after preliminary experiments (data not shown). On the day of synthesis, sections were warmed to room temperature, air-dried, and then preincubated in a 0.1 M phosphate-buffered saline solution (pH 7.4) for 20 min. Tissue was then air-dried once more and incubated with 48.2 MBq/L of [^{11}C]-(*R*)-**3** (107 GBq/μmol) alone (baseline) or [^{11}C]-(*R*)-**3** + **5** 10 μM (blocking) in the same buffer solution at room temperature for 60 min. After incubation, slides were dipped three

times in buffer and one time in water in distilled water (4°C) and dried under a stream of cool air. The sections were then exposed on a radioluminographic imaging plate (Fujifilm BAS-MS2025) for 3 h (Supplementary Fig. S6). The drawn ROIs obtained from histological staining of adjacent sections as previously described were then transposed to the corresponding autoradiography images. Activity in photostimulated luminescence unit per mm^2 was calculated for each ROI using Image Gauge 4.0 (Fujifilm). Grey and white matter binding were averaged. Group differences in binding were then investigated using a one-way ANOVA and specific binding was analyzed using an unpaired two-tailed Student t test for each ROI.

PET/MR Imaging Study in Human Subject*. Imaging procedure.* Dynamic PET data were acquired on a Siemens Biograph 64 True Point PET/CT scanner (Siemens Medical Solutions, Erlangen, Germany) at the Department of Nuclear Medicine, University of Munich (LMU) with an injection of 567 MBq of [^{11}C]-(R)-**3**. Reconstruction included standard corrections for attenuation (low dose CT), scatter, decay and random counts. Dynamic PET data were recorded in list mode over 60 min and reconstructed using a 3D ordered subsets expectation maximization (OSEM) algorithm with 4 iterations and 8 subsets, followed by a Gaussian filter with five millimeters FWHM. The study was realized in a 256 x 256 x 109 matrix with zoom 2 (voxel size of 1.336 × 1.336 × 2.027) in 30 time frames (12 × 10, 4 × 30, 2 × 60, 2 × 120, 10 × 300 s). A correction of patient motion between time frames was performed using the PMOD Fusion tool (v3.4, PMOD Technologies, Zurich, Switzerland). *Image analyses.* Anatomical brain regions were defined in the OSEM3D reconstructions with PMOD Neuro tool (v3.4 PMOD Technologies, Zurich, Switzerland) based on the Hammers maximum probability atlas (Hammers N30R83)[63]. Mean SUV values for 0-10, 10-30, 30-60 min p.i. averaged images were derived For this anatomical comparison a T1 MP-RAGE MR image of the subject with isotropic voxels recorded on a 3 Tesla scanner (Magnetom Trio, Siemens, Erlangen) equipped with a 32-channel head coil was used. The production of [^{11}C]-(R)-**3** was performed in accordance with the German

Medical Products Act AMG §13 2b and administration was done following consultation of the local ethical committee

ASSOCIATED CONTENT

Supporting Information Available:

Supplementary tables and figures, chiral SFC/MS analyses of (±)-**12**, (*R*)-**12** and (*S*)-**12**, crystallographic data for compound (R_S,*R*)-**9**, detailed methods for biological evaluation, radiochemistry and NMR spectra (PDF)

Molecular formula strings and some data (CSV)

AUTHOR INFORMATION

Vadim Bernard-Gauthier. E-mail: bernardg@ualberta.ca. Phone: 780-248-5660.

ORCID

Vadim Bernard-Gauthier: 0000-0002-1588-7981

Prof. Ralf Schirrmacher. E-mail: schirrma@ualberta.ca. Phone: 780-248-1829.

ORCID

Ralf Schirrmacher: 0000-0002-7098-3036

ACKNOWLEDGEMENTS

We thank Dr. Esther Schirrmacher for reading the manuscript and providing useful comments. We are thankful to Angelina Morales-Izquierdo, Karine Gilbert and Alexandra Furtos for the mass spectrometry and SFC analyses. We are also grateful to Dave Clendening and Blake Lazurko from the Edmonton PET Centre and Gassan Massarweh and Dean Jolly from the Montreal Neurological Institute for radionuclide production. We thank Michel Simard for the X-ray crystallographic service. We are also grateful to Frank Wuest for access to radiochemistry laboratory for the small animal PET imaging work. We also thank Prof. Sibylle Ziegler. This work

was financially supported by Canada Foundation for Innovation (CFI) project no. 203639 to R.S, Cancer Research Society and C^7 Council to RS, Natural Science and Engineering Research Council of Canada (NSERC) to RS and Weston Brain Institute to RS and US Department of Energy / National Institute of Biomedical Imaging and Bioengineering (DE-SC0012484) to PJHS.

COMPETING FINANCIAL INTERESTS

The authors declare no competing financial interests.

ABBREVIATION USED

AD, Alzheimer's disease; A_m, molar activity; BBB, blood-brain barrier; BCRP, breast cancer resistance protein; BDNF, brain-derived neurotrophic factor; B_{avail}, concentration of free receptors; B_{max}, total density of receptors; CNS, central nervous system; CT, computed tomography; GMP, good manufacturing practice; GPCR, G protein-coupled receptor; HC, healthy control; IHC, immunohistochemistry ; ISH, in situ hybridization; K_p, brain-to-blood ratio; MDCKII, Madin-Darby canine kidney; NGF, nerve growth factor; NGS, next-generation sequencing; NT-3, neurotrophin-3; NTRK, neurotrophic tyrosine kinase; PET, positron emission tomography; P-gp, P-glycoprotein; PNS, peripheral nervous system; RB, rotatable bond; ROI, region of interest; SAR, structure-activity relationship; SUV, standardized uptake values; TK, tyrosine kinase; TKI, tyrosine kinase inhibitor; TPSA, topological polar surface area; Trk, tropomyosin receptor kinase.

REFERENCES

1. Chao, M. V. Neurotrophins and their receptors: a convergence point for many signalling pathways. *Nat. Rev. Neurosci.* **2003**, *4*, 299-309.

2. Chao, M. V. Neurotrophin Receptors - a window into neuronal differentiation. *Neuron* **1992**, *9*, 583-593.

3. Deinhardt K, C. M. Trk receptors. *Handb. Exp. Pharmacol.* **2014**, *220*, 103-119.

4. Oyesiku, N. M.; Evans, C. O.; Houston, S.; Darrell, R. S.; Smith, J. S.; Fulop, Z. L.; Dixon, C. E.; Stein, D. G. Regional changes in the expression of neurotrophic factors and their receptors following acute traumatic brain injury in the adult rat brain. *Brain Res.* **1999**, *833*, 161-172.

5. Ray, M. T.; Weickert, C. S.; Webster, M. J. Decreased BDNF and TrkB mRNA expression in multiple cortical areas of patients with schizophrenia and mood disorders. *Transl. Psychiatry* **2014**, *4*, e389.

6. Reinhart, V.; Bove, S. E.; Volfson, D.; Lewis, D. A.; Kleiman, R. J.; Lanz, T. A. Evaluation of TrkB and BDNF transcripts in prefrontal cortex, hippocampus, and striatum from subjects with schizophrenia, bipolar disorder, and major depressive disorder. *Neurobiol. Dis.* **2015**, *77*, 220-227.

7. Deng, V.; Matagne, V.; Banine, F.; Frerking, M.; Ohliger, P.; Budden, S.; Pevsner, J.; Dissen, G. A.; Sherman, L. S.; Ojeda, S. R. FXYD1 is an MeCP2 target gene overexpressed in the brains of Rett syndrome patients and Mecp2-null mice. *Hum. Mol. Genet.* **2007**, *16*, 640-650.

8. Gines, S.; Bosch, M.; Marco, S.; Gavalda, N.; Diaz-Hernandez, M.; Lucas, J. J.; Canals, J. M.; Alberch, J. Reduced expression of the TrkB receptor in Huntington's disease mouse models and in human brain. *Eur. J. Neurosci.* **2006**, *23*, 649-658.

9. Fumagalli, F.; Racagni, G.; Riva, M. A. Shedding light into the role of BDNF in the pharmacotherapy of Parkinson's disease. *Pharmacogenomics J.* **2006**, *6*, 95-104.

10. Nagahara, A. H.; Tuszynski, M. H. Potential therapeutic uses of BDNF in neurological and psychiatric disorders. *Nat. Rev. Drug Discovery* **2011**, *10*, 209-219.

11. Ginsberg, S. D.; Che, S. L.; Wuu, J.; Counts, S. E.; Mufson, E. J. Down regulation of trk but not p75(NTR) gene expression in single cholinergic basal forebrain neurons mark the progression of Alzheimer's disease. *J.Neurochem.* **2006**, *97*, 475-487.

12. Ferrer, I.; Marin, C.; Rey, M. J.; Ribalta, T.; Goutan, E.; Blanco, R.; Tolosa, E.; Marti, E. BDNF and full-length and truncated TrkB expression in Alzheimer disease. Implications in therapeutic strategies. *J. Neuropath. Exp. Neur.* **1999**, *58*, 729-739.

13. Allen, S. J.; Wilcock, G. K.; Dawbarn, D. Profound and selective loss of catalytic TrkB immunoreactivity in Alzheimer's disease. *Biochem. Biophys. Res. Commun.* **1999**, *264*, 648-651.

14. Zhang, F.; Kang, Z. L.; Li, W.; Xiao, Z. C.; Zhou, X. F. Roles of brain-derived neurotrophic factor/tropomyosin-related kinase B (BDNF/TrkB) signalling in Alzheimer's disease. *J. Clin. Neurosci.* **2012**, *19*, 946-949.

15. Vaishnavi, A.; Le, A. T.; Doebele, R. C. TRKing down an old oncogene in a new era of targeted therapy. *Cancer Discovery* **2015,** *5*, 25-34.

16. McCarthy, C.; Walker, E. Tropomyosin receptor kinase inhibitors: a patent update 2009-2013. *Expert Opin. Ther. Pat.* **2014**, *24*, 731-744.

17. Martin-Zanca, D.; Hughes, S. H.; Barbacid, M. A human oncogene formed by the fusion of truncated tropomyosin and protein tyrosine kinase sequences. *Nature* **1986**, *319*, 743-748.

18. Kaplan, D. R.; Hempstead, B. L.; Martin-Zanca, D.; Chao, M. V.; Parada, L. F. The Trk protooncogene product - a signal transducing receptor for nerve growth-factor. *Science* **1991**, *252*, 554-558.

19. Klein, R.; Jing, S. Q.; Nanduri, V.; Orourke, E.; Barbacid, M. The Trk protooncogene encodes a receptor for nerve growth-factor. *Cell* **1991**, *65*, 189-197.

20. Mufson, E. J.; Li, J. M.; Sobreviela, T.; Kordower, J. H. Decreased trkA gene expression within basal forebrain neurons in Alzheimer's disease. *NeuroReport* **1996**, *8*, 25-29.

21. Weickert, C. S.; Ligons, D. L.; Romanczyk, T.; Ungaro, G.; Hyde, T. M.; Herman, M. M.; Weinberger, D. R.; Kleinman, J. E. Reductions in neurotrophin receptor mRNAs in the prefrontal cortex of patients with schizophrenia. *Mol. Psychiatry* **2005**, *10*, 637-650.

22. Romanczyk, T. B.; Weickert, C. S.; Webster, M. J.; Herman, M. M.; Akil, M.; Kleinman, J. E., Alterations in trkB mRNA in the human prefrontal cortex throughout the lifespan. *Eur. J. Neurosci.* **2002**, *15*, 269-280.

23. Beltaifa, S.; Webster, M. J.; Ligons, D. L.; Fatula, R. J.; Herman, M. M.; Kleinman, J. E.; Weickert, C. S. Discordant changes in cortical TrkC mRNA and protein during the human lifespan. *Eur. J. Neurosci.* **2005**, *21*, 2433-2444.

24. Webster, M. J.; Herman, M. M.; Kleinman, J. E.; Shannon Weickert, C. BDNF and trkB mRNA expression in the hippocampus and temporal cortex during the human lifespan. *Gene Expression Patterns* **2006**, *6*, 941-951.

25. Menichincheri, M.; Ardini, E.; Magnaghi, P.; Avanzi, N.; Banfi, P.; Bossi, R.; Buffa, L.; Canevari, G.; Ceriani, L.; Colombo, M.; Corti, L.; Donati, D.; Fasolini, M.; Felder, E.; Fiorelli, C.; Fiorentini, F.; Galvani, A.; Isacchi, A.; Borgia, A. L.; Marchionni, C.; Nesi, M.; Orrenius, C.; Panzeri, A. Pesenti, E.; Rusconi, L.; Saccardo, M. B.; Vanotti, E.; Perrone, E.; Orsini, P., Discovery of Entrectinib: A new 3-aminoindazole as a potent anaplastic lymphoma kinase (ALK), c-ros oncogene 1 kinase (ROS1), and pan-tropomyosin receptor kinases (pan-TRKs) inhibitor. *J. Med. Chem.* **2016**, *59*, 3392-3408.

26. Ardini, E.; Menichincheri, M.; Banfi, P.; Bosotti, R.; De Ponti, C.; Pulci, R.; Ballinari, D.; Ciomei, M.; Texido, G.; Degrassi, A.; Avanzi, N.; Amboldi, N.; Saccardo, M. B.; Casero, D.; Orsini, P.; Bandiera, T.; Mologni, L.; Anderson, D.; Wei, G.; Harris, J.; Vernier, J. M.; Li, G.;

Felder, E.; Donati, D.; Isacchi, A.; Pesenti, E.; Magnaghi, P.; Galvani, A. Entrectinib, a pan-TRK, ROS1, and ALK inhibitor with activity in multiple molecularly defined cancer indications. *Mol. Cancer Ther.* **2016**, *15*, 628-639.

27. Van de Bittner, G. C.; Ricq, E. L.; Hooker, J. M. A philosophy for CNS radiotracer design. *Acc. Chem. Res.* **2014**, *47*, 3127-3134.

28. Zhang, L.; Villalobos, A.; Beck, E. M.; Bocan, T.; Chappie, T. A.; Chen, L.; Grimwood, S.; Heck, S. D.; Helal, C. J.; Hou, X.; Humphrey, J. M.; Lu, J.; Skaddan, M. B.; McCarthy, T. J.; Verhoest, P. R.; Wager, T. T.; Zasadny, K. Design and selection parameters to accelerate the discovery of novel central nervous system positron emission tomography (PET) ligands and their application in the development of a novel phosphodiesterase 2A PET ligand. *J. Med. Chem.* **2013,** *56*, 4568-4579.

29. Holland, J. P.; Cumming, P.; Vasdev, N. PET radiopharmaceuticals for probing enzymes in the brain. *Am. J. Nucl. Med. Mol. Imaging* **2013**, *3*, 194-216.

30. Wey, H. Y.; Gilbert, T. M.; Zurcher, N. R.; She, A.; Bhanot, A.; Taillon, B. D.; Schroeder, F. A.; Wang, C. G.; Haggarty, S. J.; Hooker, J. M. Insights into neuroepigenetics through human histone deacetylase PET imaging. *Sci. Transl. Med.* **2016**, *8* (351).

31. Frisen, J.; Verge, V. M. K.; Fried, K.; Risling, M.; Persson, H.; Trotter, J.; Hokfelt, T.; Lindholm, D. Characterization of glial Trkb receptors - differential response to injury in the central and peripheral nervous systems. *Proc. Natl. Acad. Sci. U. S. A.* **1993**, *90* , 4971-4975.

32. Rose, C. R.; Blum, R.; Pichler, B.; Lepier, A.; Kafitz, K. W.; Konnerth, A. Truncated TrkB-T1 mediates neurotrophin-evoked calcium signalling in glia cells. *Nature* **2003**, *426*, 74-78.

33. Pike, V. W., PET radiotracers: crossing the blood-brain barrier and surviving metabolism. *Trends Pharmacol. Sci.* **2009**, *30*, 431-440.

34. Rankovic, Z. CNS drug design: Balancing physicochemical properties for optimal brain exposure. *J. Med. Chem.* **2015**, *58*, 2584-2608.

35. Wager, T. T.; Hou, X. J.; Verhoest, P. R.; Villalobos, A. Moving beyond rules: The development of a central nervous system multiparameter optimization (CNS MPO) approach to enable alignment of druglike properties. *ACS Chem. Neurosci.* **2010**, *1*, 435-449.

36. Bernard-Gauthier, V.; Bailey, J. J.; Aliaga, A.; Kostikov, A.; Rosa-Neto, P.; Wuest, M.; Brodeur, G. M.; Bedell, B. J.; Wuest, F.; Schirrmacher, R. Development of subnanomolar radiofluorinated (2-pyrrolidin-1-yl)imidazo[1,2-b]pyridazine pan-Trk inhibitors as candidate PET imaging probes. *MedChemComm* **2015**, *6*, 2184-2193.

37. Bernard-Gauthier, V.; Aliaga, A.; Aliaga, A.; Boudjemeline, M.; Hopewell, R.; Kostikov, A.; Rosa-Neto, P.; Thiel, A.; Schirrmacher, R. Syntheses and evaluation of carbon-11 and fluorine-18-radiolabeled pan-tropomyosin receptor kinase (Trk) inhibitors: exploration of the 4-aza-2-oxindole scaffold as Trk PET imaging agents. *ACS Chem. Neurosci.* **2015,** *6*, 260-276.

38. Choi, H. S.; Rucker, P. V.; Wang, Z. C.; Fan, Y.; Albaugh, P.; Chopiuk, G.; Gessier, F.; Sun, F. X.; Adrian, F.; Liu, G. X.; Hood, T.; Li, N. X.; Jia, Y.; Che, J. W.; McCormack, S.; Li, A.; Li, J.; Steffy, A.; Culazzo, A.; Tompkins, C.; Phung, V.; Kreusch, A.; Lu, M.; Hu, B.; Chaudhary, A.; Prashad, M.; Tuntland, T.; Liu, B.; Harris, J.; Seidel, H. M.; Loren, J.; Molteni, V. (R)-2-Phenylpyrrolidine substituted imidazopyridazines: A new class of potent and selective pan-TRK inhibitors. *ACS Med. Chem. Lett.* **2015**, *6*, 562-567.

39. Haas, J.; Andrews, S. W.; Jiang, Y.; Zhang, G. Substituted pyrazolo[1,5a]pyrimidine compounds as Trk kinase inhibitors. WO/2010/048314 A1; International application No. PCT/US2009/061519. 2010.

40. Reddy, L. R.; Prashad, M. Asymmetric synthesis of 2-substituted pyrrolidines by addition of Grignard reagents to gamma-chlorinated N-tert-butanesulfinyl imine. *Chem. Commun.* **2010**, *46*, 222-224.

41. Cheng, Y.; Prusoff, W. H. Relationship between the inhibition constant (K1) and the concentration of inhibitor which causes 50 per cent inhibition (I50) of an enzymatic reaction. *Biochem. Pharmacol.* **1973**, *22*, 3099-3108.

42. Knight, Z. A.; Shokat, K. M. Features of selective kinase inhibitors. *Chem. Biol.* **2005**, *12*, 621-637.

43. Altar, C. A.; Siuciak, J. A.; Wright, P.; Ip, N. Y.; Lindsay, R. M.; Wiegand, S. J. In-situ hybridization of Trkb and Trkc receptor messenger-rna in rat forebrain and association with high-affinity binding of [I-125] Bdnf, [I-125] Nt-4/5 and [I-125] Nt-3. *Eur. J. Neurosci.* **1994**, *6*, 1389-1405.

44. Weiss, G. J.; Hidalgo, M.; Borad, M. J.; Laheru, D.; Tibes, R.; Ramanathan, R. K.; Blaydorn, L.; Jameson, G.; Jimeno, A.; Isaacs, J. D.; Scaburri, A.; Pacciarini, M. A.; Fiorentini, F.; Ciomei, M.; Von Hoff, D. D. Phase I study of the safety, tolerability and pharmacokinetics of PHA-848125AC, a dual tropomyosin receptor kinase A and cyclin-dependent kinase inhibitor, in patients with advanced solid malignancies. *Invest. New Drugs* **2012**, *30*, 2334-2343.

45. Skerratt, S. E.; Andrews, M.; Bagal, S. K.; Bilsland, J.; Brown, D.; Bungay, P. J.; Cole, S.; Gibson, K. R.; Jones, R.; Morao, I.; Nedderman, A.; Omoto, K.; Robinson, C.; Ryckmans, T.; Skinner, K.; Stupple, P.; Waldron, G. The discovery of a potent, selective, and peripherally restricted pan-Trk inhibitor (PF-06273340) for the treatment of pain. *J. Med. Chem.* **2016**, *59*, 10084-10099.

46. Doebele, R. C.; Davis, L. E.; Vaishnavi, A.; Le, A. T.; Estrada-Bernal, A.; Keysar, S.; Jimeno, A.; Varella-Garcia, M.; Aisner, D. L.; Li, Y. L.; Stephens, J.; Morosini, D.; Tuch, B. B.; Fernandes, M.; Nanda, N.; Low, J. A. An oncogenic NTRK fusion in a patient with soft-tissue sarcoma with response to the tropomyosin-related kinase inhibitor LOXO-101. *Cancer Discovery* **2015**, *5*, 1049-1057.

47. Farago, A. F.; Le, L. P.; Zheng, Z.; Muzikansky, A.; Drilon, A.; Patel, M.; Bauer, T. M.; Liu, S. V.; Ou, S. H.; Jackman, D.; Costa, D. B.; Multani, P. S.; Li, G. G.; Hornby, Z.; Chow-

Maneval, E.; Luo, D.; Lim, J. E.; Iafrate, A. J.; Shaw, A. T. Durable clinical response to Entrectinib in NTRK1-rearranged non-small cell lung cancer. *J. Thorac. Oncol.* **2015**, *10*, 1670-1674.

48. Syvanen, S.; Lindhe, O.; Palner, M.; Kornum, B. R.; Rahman, O.; Langstrom, B.; Knudsen, G. M.; Hammarlund-Udenaes, M. Species differences in blood-brain transport of three positron emission tomography radioligands with emphasis on P-glycoprotein transport. *Drug Metab. Dispos.* **2009**, *37*, 635-643.

49. Deo, A. K.; Theil, F. P.; Nicolas, J. M. Confounding parameters in preclinical assessment of blood-brain barrier permeation: An overview with emphasis on species differences and effect of disease states. *Mol. Pharmaceutics* **2013**, *10*, 1581-1595.

50. Savaskan, E.; Muller-Spahn, F.; Olivieri, G.; Bruttel, S.; Otten, U.; Rosenberg, C.; Hulette, C.; Hock, C. Alterations in trk A, trk B and trk C receptor immunoreactivities in parietal cortex and cerebellum in Alzheimer's disease. *Eur. Neurol.* **2000**, *44*, 172-180.

51. Altar, C. A.; Burton, L. E.; Bennett, G. L.; Dugichdjordjevic, M. Recombinant human nerve growth-factor is biologically-active and labels novel high-affinity binding-sites in rat brain. *Proc. Natl. Acad. Sci. U. S. A.* **1991**, *88*, 281-285.

52. Birchmeier, C.; Sharma, S.; Wigler, M. Expression and rearrangement of the ROS1 gene in human glioblastoma cells. *Proc. Natl. Acad. Sci. U. S. A.* **1987**, *84*, 9270-9274.

53. Cozza, A.; Melissari, E.; Iacopetti, P.; Mariotti, V.; Tedde, A.; Nacmias, B.; Conte, A.; Sorbi, S.; Pellegrini, S. SNPs in neurotrophin system genes and Alzheimer's disease in an Italian population. *J. Alzheimers Dis.* **2008**, *15*, 61-70.

54. Vepsalainen, S.; Castren, E.; Helisalmi, S.; Iivonen, S.; Mannermaa, A.; Lehtovirta, M.; Hanninen, T.; Soininen, H.; Hiltunen, M. Genetic analysis of BDNF and TrkB gene polymorphisms in Alzheimer's disease. *J. Neurol.* **2005**, *252*, 423-428.

55. Castello, N. A.; Nguyen, M. H.; Tran, J. D.; Cheng, D.; Green, K. N.; LaFerla, F. M. 7,8-Dihydroxyflavone, a small molecule TrkB agonist, improves spatial memory and increases thin

spine density in a mouse model of alzheimer disease-like neuronal loss. *PLoS One* **2014**, *9*, 91453.

56. Li, N.; Liu, G. T. The novel squamosamide derivative FLZ enhances BDNF/TrkB/CREB signaling and inhibits neuronal apoptosis in APP/PS1 mice. *Acta Pharmacol. Sin.* **2010**, *31*, 265-272.

57. Massa, S. M.; Yang, T.; Xie, Y. M.; Shi, J.; Bilgen, M.; Joyce, J. N.; Nehama, D.; Rajadas, J.; Longo, F. M. Small molecule BDNF mimetics activate TrkB signaling and prevent neuronal degeneration in rodents. *J. Clin. Invest.* **2010**, *120*, 1774-1785.

58. Liang, S. H.; Chen, J.M.; Normandin, M. D.; Chang, J. S.; Chang, G. C.; Taylor, C. K.; Trapa, P.; Plummer, M. S.; Para, K. S.; Conn, E. L.; Lopresti-Morrow, L.; Lanyon, L. F.; Cook, J. M.; Richter, K. E.; Nolan, C. E.; Schachter, J. B.; Janat, F.; Che, Y.; Shanmugasundaram, V.; Lefker, B. A.; Enerson, B. E.; Livni, E.; Wang, L.; Guehl, N. J.; Patnaik, D.; Wagner, F. F.; Perlis, R.; Holson, E. B.; Haggarty, S. J.; El Fakhri, G.; Kurumbail, R. G.; Vasdev, N. Discovery of a highly selective glycogen synthase kinase-3 inhibitor (PF-04802367) that modulates Tau phosphorylation in the brain: Translation for PET neuroimaging. *Angew. Chem. Int. Ed. Engl.* **2016**, *55*, 9601-9605.

59. Bailey, J. J. S., R.; Farrell, K.; Bernard-Gauthier, V. Tropomyosin receptor kinase inhibitors: an updated patent review 2010-2016 Part 1. *Expert Opin. Ther. Patents* **2017**, *27,* 733-751.

60. Bailey, J. J. S., R.; Farrell, K.; Bernard-Gauthier, V. Tropomyosin receptor kinase inhibitors: an updated patent review 2010-2016 Part 2. *Expert Opin. Ther. Patents* **2017**, *27,* 831-849.

61. Bauer, B.; Miller, D. S.; Fricker, G. Compound profiling for p-glycoprotein at the blood-brain barrier using a microplate screening system. *Pharm. Res.* **2003**, *20*, 1170-1176.

62. Mahringer, A.; Delzer, J.; Fricker, G. A fluorescence-based in vitro assay for drug interactions with breast cancer resistance protein (BCRP, ABCG2). *Eur. J. Pharm. Biopharm.* **2009**, *72*, 605-613.

63. Hammers, A.; Allom, R.; Koepp, M. J.; Free, S. L.; Myers, R.; Lemieux, L.; Mitchell, T. N.; Brooks, D. J.; Duncan, J. S. Three-dimensional maximum probability atlas of the human brain, with particular reference to the temporal lobe. *Hum. Brain Mapp.* **2003**, *19*, 224-47.

FIGURES LEGENDS

Figure 1. Chemical structures of pan-Trk selective type-I PET radiotracers and Trk kinase inhibitors under clinical evaluation for the treatment of solid tumors.

Figure 2. Binding mode, potency/affinity and kinome selectivity profiling of (*R*)-3. (a) View of the predicted type-I binding mode of (*R*)-**3** with TrkA (grey ribbons, PDB: 4PMT) overlaid onto the X-ray crystal structure of TrkB (DFG-in conformation, cyan ribbons, PDB: 4AT3). (b) Surface rendering of (*R*)-**3** bound to the ATP binding site of TrkA illustrating the overlap between the 2-fluorophenylpyrrolidine moiety and the ribose pocket. (c) Dose-response curve for inhibitor (*R*)-**3** versus TrkA, TrkB, TrkC, ACK1, ROS1 and TXK (1 μM ATP, n = 1). (d) Dose-response curve for inhibitor (*R*)-**3** versus TrkA, TrkB, TrkC, ([ATP] = $K_{m\ ATP}$, n = 3, error bars represent standard deviation from the mean). (e) Comprehensive kinase selectivity profile of (*R*)-**3** against 369 kinases (Kinases are ordered alphabetically and data represented as radar chart with 100.0%, 50.0% and 0 % activity relative to control (200 nM, n = 2) ([γ-^{33}P]ATP-based enzymatic assay performed by Reaction Biology).

Figure 3. **Preclinical *in vivo* PET imaging of [^{11}C]-(±)-3, [^{11}C]-(*R*)-3 and [^{11}C]5 in FVB and Mdr1a/b$^{(-/-)}$Bcrp1$^{(-/-)}$ mice, [^{11}C]-(*R*)-3 *in vivo* stability and blocking studies**. CB, cerebellum; Ctx, cortex; HY, hypothalamus; OB, olfactory bulb; TH, thalamus. Expressed as mean ± SD. (a) Representative brain images of [^{11}C]-(±)-**3** in FVB mice. (b) Representative brain images of [^{11}C]-(±)-**3** in Mdr1a/b$^{(-/-)}$Bcrp1$^{(-/-)}$ mice. (c) Representative brain images of [^{11}C]-(*R*)-**3** in FVB mice. (d) Representative brain images of [^{11}C]-(*R*)-3 in Mdr1a/b$^{(-/-)}$Bcrp1$^{(-/-)}$ mice. (e) TACs for [^{11}C]-(±)-**3** brain uptake at baseline (n = 3/group). (f) TACs for [^{11}C]-(*R*)-**3** brain uptake at baseline (n = 3/group). (g) Selected biodistribution data presenting the accumulation of [^{11}C]-(*R*)-**3** in liver, kidneys, blood (heart), lung in comparison to brain over the duration the scans (n = 3; checkered colors = FVB mice; full colors = Mdr1a/b$^{(-/-)}$Bcrp1$^{(-/-)}$ mice). (h) *NTRK2*

transcripts analyzed by *in situ* hybridization in the Allen Brain Atlas project. Images are taken from the Allen Brain Atlas (http://mouse.brain-map.org). Image credit: Allen Institute for Brain Science. (i) *In vivo* [^{11}C]-(*R*)-**3** stability and metabolite composition at 5, 15 and 30 min post injection in FVB mouse (*n* = 1) with corresponding radio-TLC (plasma). (j) Representative brain images of [^{11}C]**5** in FVB mice. (k) Representative brain images of [^{11}C]**5** in Mdr1a/b$^{(-/-)}$Bcrp1$^{(-/-)}$ mice. (l) TACs for [^{11}C]**5** brain exposition at baseline (*n* = 3/group). (m) Selected biodistribution data presenting the accumulation of [^{11}C]**5** in liver, kidneys, blood (heart), lung in comparison to brain over the duration the scans (*n* = 3; checkered colors = FVB mice; full colors = Mdr1a/b$^{(-/-)}$Bcrp1$^{(-/-)}$ mice). (n) Predicted binding mode of entrecitnib (green sticks) overlaid onto the binding of (*R*)-**3** (yellow sticks) (TrkA; grey, PDB: 4PMT and TrkB; cyan, PDB: 4AT3). (o) Representative brain images of [^{11}C]-(*R*)-**3** in FVB mice following pretreatment with vehicle (DMSO, 100 μL, 30 min pre-dosed i.p.). (p) Representative brain images of [^{11}C]-(*R*)-**3** in FVB mice following pretreatment with 50 mg/kg entrectinib (DMSO solution, 100 μL, 30 min pre-dosed i.p.). (q) Representative brain images of [^{11}C]-(*R*)-**3** in FVB mice following pretreatment with 350 mg/kg entrectinib (DMSO solution, 100 μL, 30 min pre-dosed i.p.). (r) TACs for [^{11}C]-(*R*)-**3** brain uptake with entrectinib pretreatment in comparison to vehicle (*n* = 1/group).

Figure 4. ***In vivo* PET imaging of [^{11}C]-(*R*)-3, [^{11}C]-(±)-3 and [^{11}C]5 in the rhesus monkey brain**. CB, cerebellum; CC, corpus callosum; Ctx, cortex; TH, thalamus. (a) Representative *in vivo* PET images of [^{11}C]-(*R*)-**3**. (b) Representative *in vivo* PET images of [^{11}C]-(±)-**3**. (c) Representative *in vivo* PET images of [^{11}C]**5**. (d) Comparative regional SUV ratio (SUVR, summed 30-60 min) for [^{11}C]-(*R*)-**3** (*n* = 3), [^{11}C]-(±)-**3** (*n* = 3) and [^{11}C]**5** (*n* = 1). [^{11}C]-(*R*)-**3** displays higher gray-to-white matter SUVR compared to [^{11}C]-(±)-**3** and [^{11}C]**5**.

Figure 5. **Regional quantification for the *in vitro* human brain tissue autoradiography experiments with [^{11}C]-(*R*)-3**. Quantification for the hippocampus (*n* = 11-12) (a,b), inferior parietal cortex (*n* = 12-15) (c,d), prefrontal cortex (*n* = 12-15) (e,f) and cerebellum (*n* = 11-15)

(g,h) for baseline ([^{11}C]-(*R*)-**3**) and blocking ([^{11}C]-(*R*)-**3** + **5**, 10 μM)) of healthy control (black) and AD (blue) human brain cryosections. PSL/mm^2 = photo-stimulated luminescence events per square millimetre. Specific binding$_{Ctr/AD}$ = Total$_{Ctr/AD}$ – Block$_{Ctr/AD}$. Expressed as mean ± SD. ***$P \leq 0.001$, ****$P \leq 0.0001$.

Figure 6. ***In vivo* PET imaging of [^{11}C]-(*R*)-3 in the human brain.** Top row: static SUV images averaged over 10-30 min p.i. of the human subject illustrating the distribution of TrkB/C. The highest values are observed in the thalamus, followed by cerebellum and cortical gray matter, with low values in white matter. Middle row: fusion with the subject MR for anatomic localization. Bottom row: T1 MP-RAGE MR image of the subject.

FIGURES

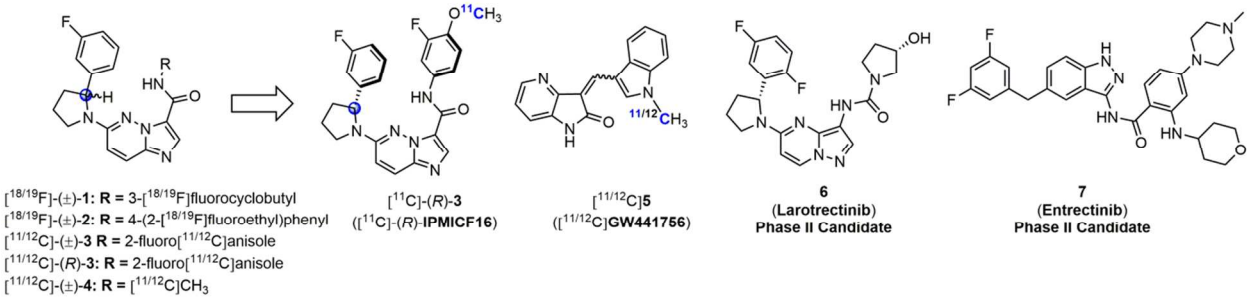

Figure 1. Chemical structures of pan-Trk selective type-I PET radiotracers and Trk kinase inhibitors under clinical evaluation for the treatment of solid tumors.

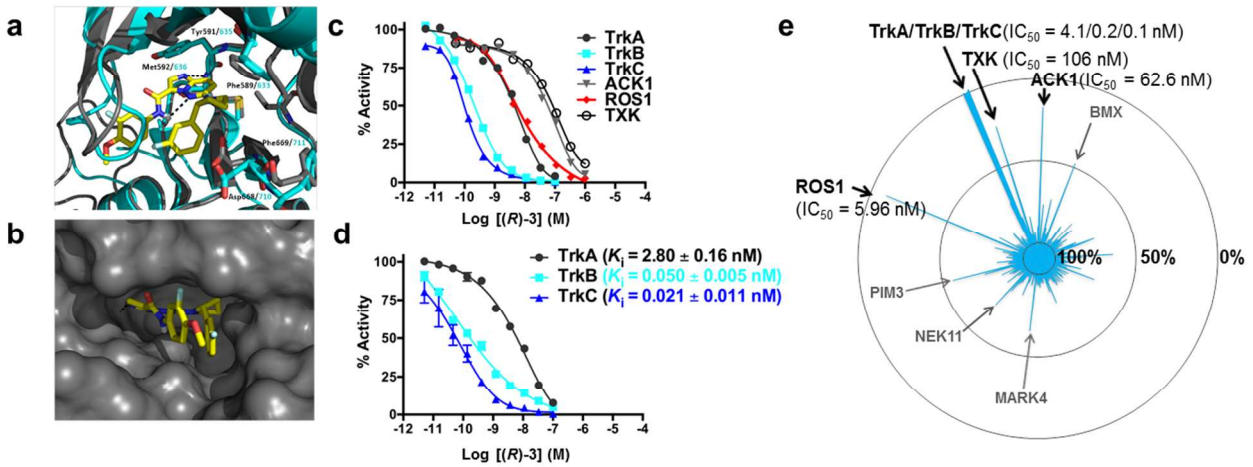

Figure 2. Binding mode, potency/affinity and kinome selectivity profiling of (*R*)-3. (a) View of the predicted type-I binding mode of (*R*)-**3** with TrkA (grey ribbons, PDB: 4PMT) overlaid onto the X-ray crystal structure of TrkB (DFG-in conformation, cyan ribbons, PDB: 4AT3). (b) Surface rendering of (*R*)-**3** bound to the ATP binding site of TrkA illustrating the overlap between the 2-fluorophenylpyrrolidine moiety and the ribose pocket. (c) Dose-response curve for inhibitor (*R*)-**3** versus TrkA, TrkB, TrkC, ACK1, ROS1 and TXK (1 μM ATP, n = 1). (d) Dose-response curve for inhibitor (*R*)-**3** versus TrkA, TrkB, TrkC, ([ATP] = $K_{m\ ATP}$, n = 3, error bars represent standard deviation from the mean). (e) Comprehensive kinase selectivity profile of (*R*)-**3** against 369 kinases (Kinases are ordered alphabetically and data represented as radar chart with 100.0%, 50.0% and 0 % activity relative to control (200 nM, n = 2) ([γ-^{33}P]ATP-based enzymatic assay performed by Reaction Biology).

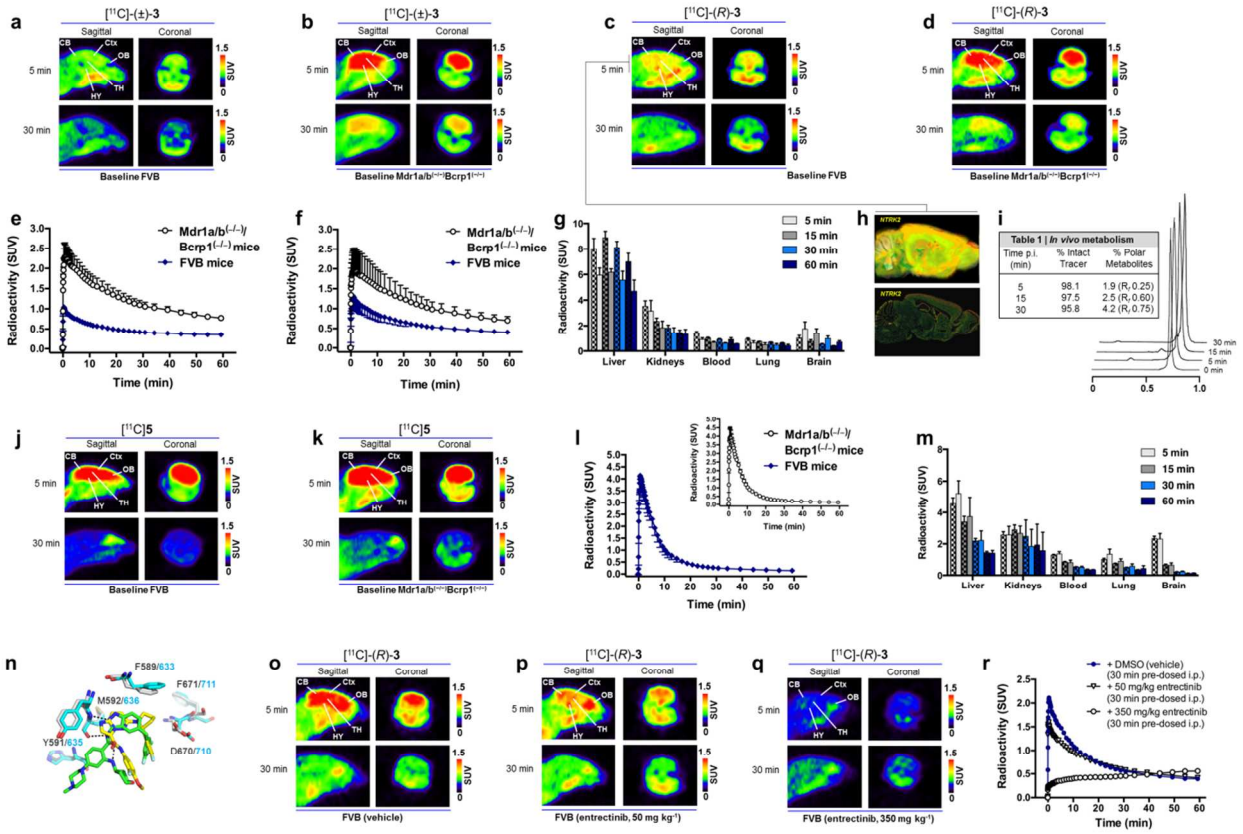

Figure 3. **Preclinical *in vivo* PET imaging of [^{11}C]-(±)-3, [^{11}C]-(*R*)-3 and [^{11}C]5 in FVB and Mdr1a/b$^{(-/-)}$Bcrp1$^{(-/-)}$ mice, [^{11}C]-(*R*)-3 *in vivo* stability and blocking studies**. CB, cerebellum; Ctx, cortex; HY, hypothalamus; OB, olfactory bulb; TH, thalamus. Expressed as mean ± SD. (a) Representative brain images of [^{11}C]-(±)-**3** in FVB mice. (b) Representative brain images of [^{11}C]-(±)-**3** in Mdr1a/b$^{(-/-)}$Bcrp1$^{(-/-)}$ mice. (c) Representative brain images of [^{11}C]-(*R*)-**3** in FVB mice. (d) Representative brain images of [^{11}C]-(*R*)-3 in Mdr1a/b$^{(-/-)}$Bcrp1$^{(-/-)}$ mice. (e) TACs for [^{11}C]-(±)-**3** brain uptake at baseline (*n* = 3/group). (f) TACs for [^{11}C]-(*R*)-**3** brain uptake at baseline (*n* = 3/group). (g) Selected biodistribution data presenting the accumulation of [^{11}C]-(*R*)-**3** in liver, kidneys, blood (heart), lung in comparison to brain over the duration the scans (*n* = 3; checkered colors = FVB mice; full colors = Mdr1a/b$^{(-/-)}$Bcrp1$^{(-/-)}$ mice). (h) *NTRK2* transcripts analyzed by *in situ* hybridization in the Allen Brain Atlas project. Images are taken from the Allen Brain Atlas (http://mouse.brain-map.org). Image credit: Allen Institute for Brain

Science. (i) *In vivo* [^{11}C]-(*R*)-**3** stability and metabolite composition at 5, 15 and 30 min post injection in FVB mouse (*n* = 1) with corresponding radio-TLC (plasma). (j) Representative brain images of [^{11}C]**5** in FVB mice. (k) Representative brain images of [^{11}C]**5** in Mdr1a/b$^{(-/-)}$Bcrp1$^{(-/-)}$ mice. (l) TACs for [^{11}C]**5** brain exposition at baseline (*n* = 3/group). (m) Selected biodistribution data presenting the accumulation of [^{11}C]**5** in liver, kidneys, blood (heart), lung in comparison to brain over the duration the scans (*n* = 3; checkered colors = FVB mice; full colors = Mdr1a/b$^{(-/-)}$Bcrp1$^{(-/-)}$ mice). (n) Predicted binding mode of entrecitnib (green sticks) overlaid onto the binding of (*R*)-**3** (yellow sticks) (TrkA; grey, PDB: 4PMT and TrkB; cyan, PDB: 4AT3). (o) Representative brain images of [^{11}C]-(*R*)-**3** in FVB mice following pretreatment with vehicle (DMSO, 100 μL, 30 min pre-dosed i.p.). (p) Representative brain images of [^{11}C]-(*R*)-**3** in FVB mice following pretreatment with 50 mg/kg entrectinib (DMSO solution, 100 μL, 30 min pre-dosed i.p.). (q) Representative brain images of [^{11}C]-(*R*)-**3** in FVB mice following pretreatment with 350 mg/kg entrectinib (DMSO solution, 100 μL, 30 min pre-dosed i.p.). (r) TACs for [^{11}C]-(*R*)-**3** brain uptake with entrectinib pretreatment in comparison to vehicle (*n* = 1/group).

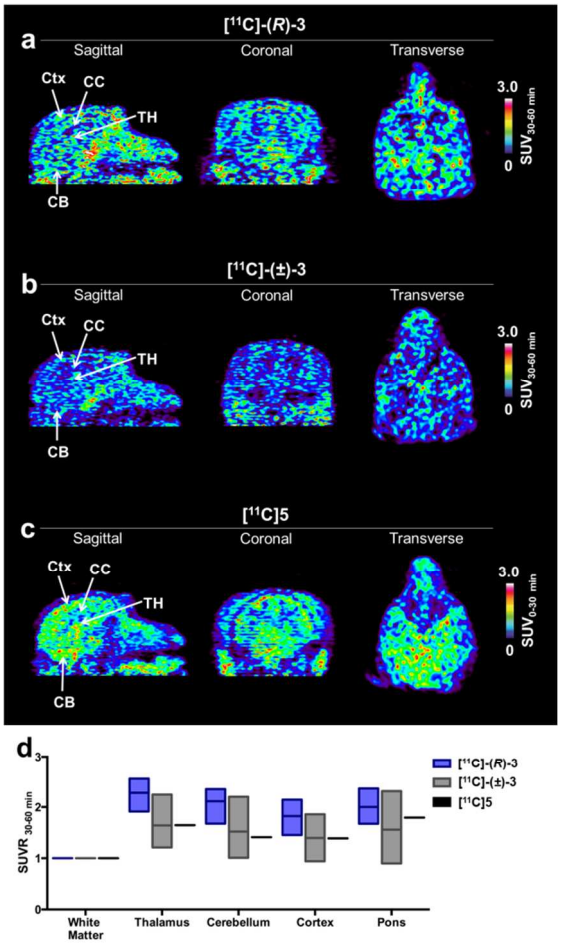

Figure 4. ***In vivo*** **PET imaging of [^{11}C]-(*R*)-3, [^{11}C]-(±)-3 and [^{11}C]5 in the rhesus monkey brain**. CB, cerebellum; CC, corpus callosum; Ctx, cortex; TH, thalamus. (a) Representative *in vivo* PET images of [^{11}C]-(*R*)-**3**. (b) Representative *in vivo* PET images of [^{11}C]-(±)-**3**. (c) Representative *in vivo* PET images of [^{11}C]**5**. (d) Comparative regional SUV ratio (SUVR, summed 30-60 min) for [^{11}C]-(*R*)-**3** (n = 3), [^{11}C]-(±)-**3** (n = 3) and [^{11}C]**5** (n = 1). [^{11}C]-(*R*)-**3** displays higher gray-to-white matter SUVR compared to [^{11}C]-(±)-**3** and [^{11}C]**5**.

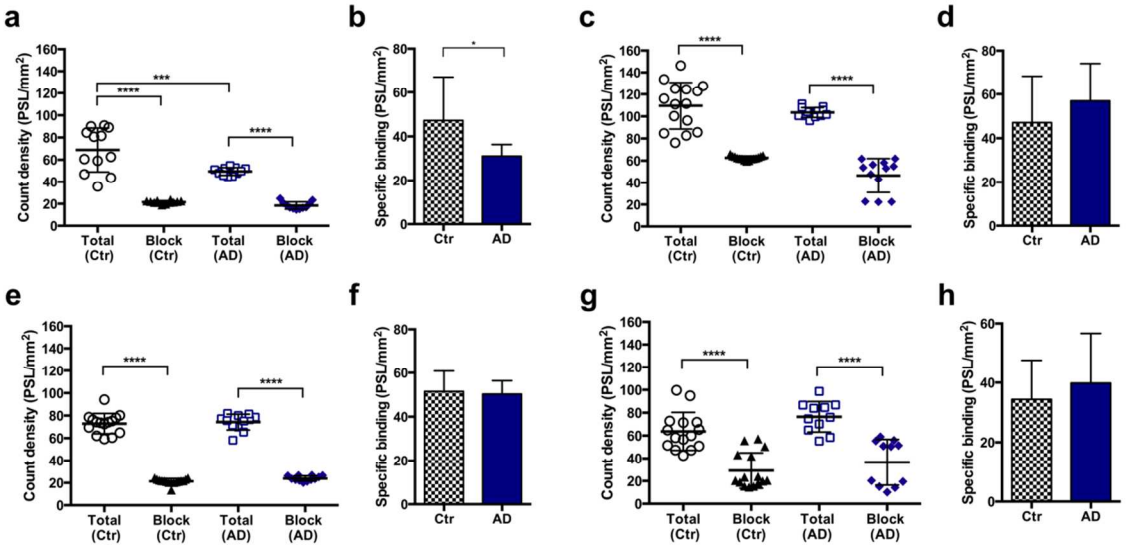

Figure 5. **Regional quantification for the *in vitro* human brain tissue autoradiography experiments with [^{11}C]-(*R*)-3**. Quantification for the hippocampus (*n* = 11-12) (a,b), inferior parietal cortex (*n* = 12-15) (c,d), prefrontal cortex (*n* = 12-15) (e,f) and cerebellum (*n* = 11-15) (g,h) for baseline ([^{11}C]-(*R*)-**3**) and blocking ([^{11}C]-(*R*)-**3** + **5**, 10 μM)) of healthy control (black) and AD (blue) human brain cryosections. PSL/mm^2 = photo-stimulated luminescence events per square millimetre. Specific binding$_{Ctr/AD}$ = Total$_{Ctr/AD}$ – Block$_{Ctr/AD}$. Expressed as mean ± SD. ***P ≤ 0.001, ****P ≤ 0.0001.

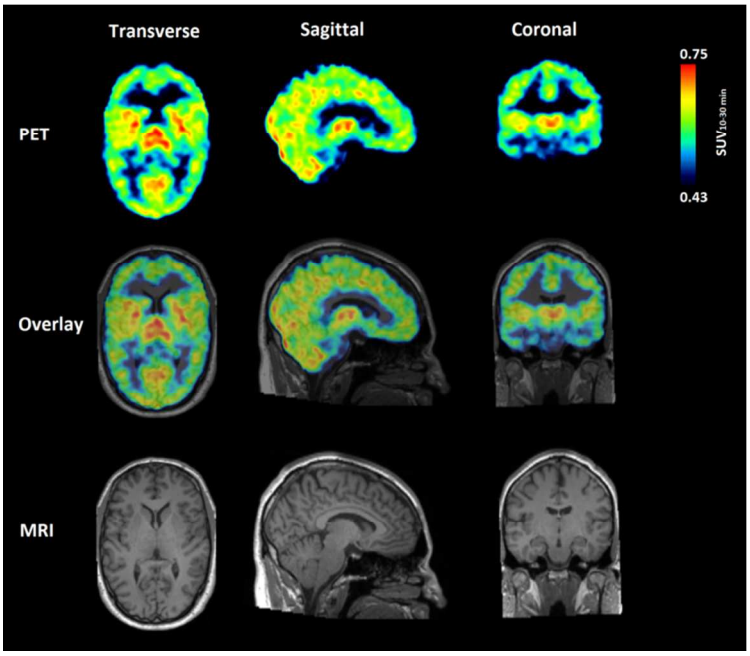

Figure 6. ***In vivo*** **PET imaging of [^{11}C]-(*R*)-3 in the human brain.** Top row: static SUV images averaged over 10-30 min p.i. of the human subject illustrating the distribution of TrkB/C. The highest values are observed in the thalamus, followed by cerebellum and cortical gray matter, with low values in white matter. Middle row: fusion with the subject MR for anatomic localization. Bottom row: T1 MP-RAGE MR image of the subject.

SCHEME

Scheme 1. Synthesis of (*R*)-**3**, radiosynthesis of [^{11}C]-(*R*)-**3** and HPLC quality control[a]

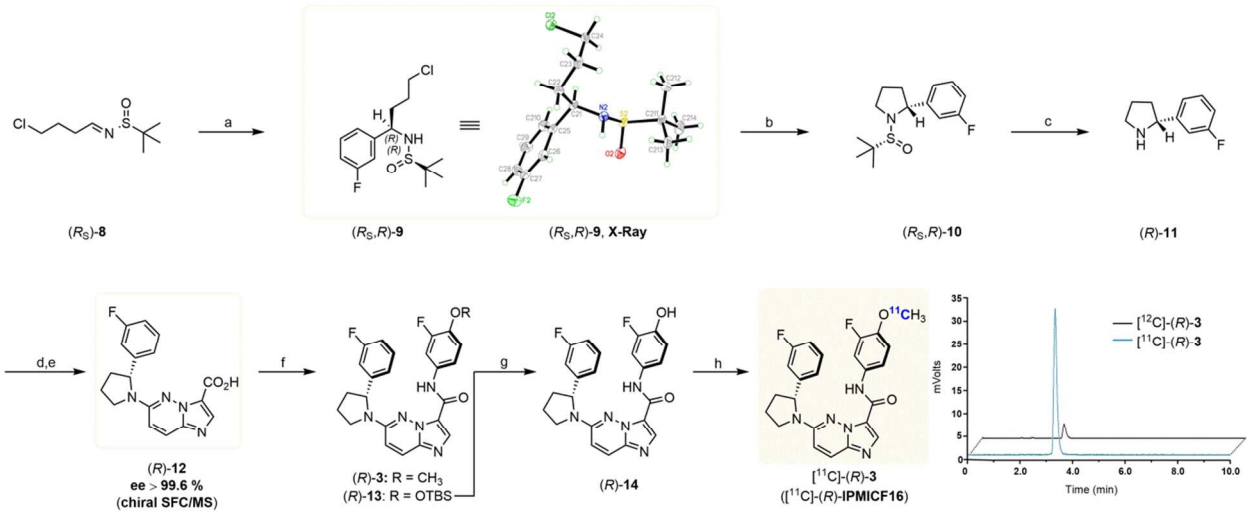

[a]Reagents and conditions: (a) 3-fluorophenylmagnesium bromide, CH_2Cl_2, -78°C – rt, 72%; (b) LiHMDS, THF, rt, 71%; (c) HCl (4N/dioxane), MeOH, rt, 99% (crude); (d) ethyl 6-chloroimidazo[1,2-*b*]pyridazine-3-carboxylate, KF, DMSO, 100°C; (e) KOH, H_2O/EtOH, rt, 55% (2 steps); (f) $ArNH_2$, DIPEA, HATU, DMF, rt, 62–99%; (g) TBAF, THF, rt, 91%; (h) [^{11}C]CH_3I, K_2CO_3 aq. sat., DMF, 3 min, 80°C *or* [^{11}C]CH_3OTf, TBAOH, DMF, 3 min, rt.

TOC graphic

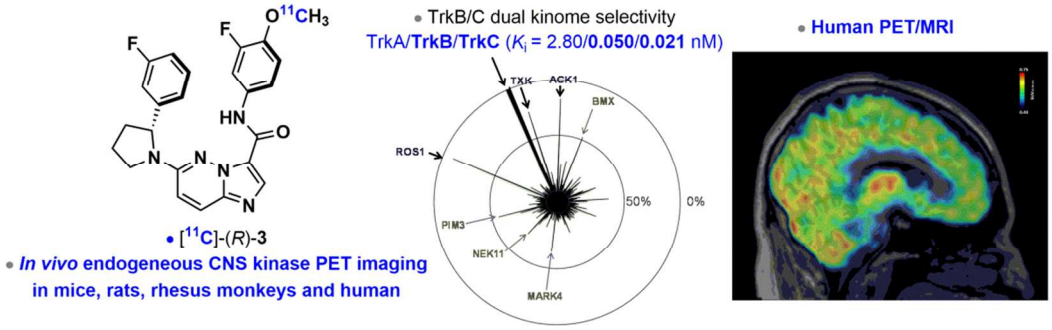
• [11C]-(R)-3
• In vivo endogeneous CNS kinase PET imaging in mice, rats, rhesus monkeys and human
• TrkB/C dual kinome selectivity
TrkA/TrkB/TrkC (Ki = 2.80/0.050/0.021 nM)
TXK
ACK1
BMX
ROS1
PIM3
NEK11
MARK4
50%
0%
• Human PET/MRI